



**University of
Zurich^{UZH}**

The Effect of Type Ia Supernova Blocking on the Estimation of the Hubble Constant

Master Thesis in Physics

Amalia Villarrubia-Aguilar

Supervised by
Prof. Dr. Julian Adamek

July 10, 2023

Abstract

The purpose of this study is to assess the bias resulting from the blocking of certain supernovae by foreground galaxies on our late-time estimation of the Hubble constant. We find that 2.4% to 9% of the supernovae in our simulated catalogue are obstructed by a foreground galaxy, depending on the way in which we define the effective radius of a galaxy. In its simplest form, this blocking implies that supernovae lying behind a foreground galaxy are excluded from our observed samples. We find that this selection bias leads to an overestimation of H_0 which ranges from 0.03% to 0.09% depending on the chosen definition for galactic radii. We show that supernova blocking also affects redshift determinations, particularly when obstructed supernovae are mistakenly assigned the redshift of their foreground galaxy instead of their host-galaxy. We find that such host-galaxy misidentifications can result in an underestimation of H_0 of the order of 1.95% if the mismatch probability is assumed to be proportional to the angular separation between the obstructed supernova and its foreground galaxy. Lastly, we examine the selection bias induced by the specific orientation of the Milky Way's plane on the estimation of the Hubble constant. Our analysis reveals that the orientation of the galactic disk alone can cause a fluctuation in the Hubble constant of ~ 0.9 km/s/Mpc when relying on low redshift sources only ($z \leq 0.1$).

Contents

1	Introduction	1
1.1	The Hubble constant under tension	1
1.2	Research motivation	5
1.2.1	Total blocking of supernovae by foreground galaxies	5
1.2.2	Supernova/host-galaxy mismatching	6
1.2.3	Supernova blocking by the Milky Way	6
2	Theoretical cosmology framework	8
2.1	The homogeneous and isotropic Universe	8
2.2	Large-scale inhomogeneities	10
2.2.1	The FLRW metric and its perturbations	11
2.2.2	The energy-momentum tensor and its perturbations	14
2.3	The Λ CDM model	15
2.3.1	Inflation	15
2.3.2	Composition of the Universe	16
2.4	Distance measures in cosmology	17
2.4.1	Theoretically-defined distances	17
2.4.2	Observable distances	19
2.4.3	The cosmological distance ladder	22
3	Estimation of the Hubble constant	24
3.1	The observed Hubble diagram	24
3.1.1	The impact of peculiar motions on the Hubble diagram	24
3.1.2	The impact of gravitational lensing on the Hubble diagram	26
3.1.3	Reconstructing an unbiased Hubble diagram	27
3.2	Markov Chain Monte Carlo (MCMC) technique for parameter inference	28
3.2.1	Bayes' Theorem	28
3.2.2	The Likelihood function	30
3.2.3	Markov Chain Monte Carlo sampling	31
4	Data	34
4.1	The simulated dark matter halo catalogue	34
4.2	Statistics of galaxy/supernova blocking	35
5	The impact of total supernova blocking on the estimation of H_0	39
5.1	Selecting an unbiased supernova sample	39
5.2	Results	40
5.3	Discussion	42

6	The impact of supernova/host-galaxy mismatching on the estimation of H_0	46
6.1	Selecting an unbiased supernova sample	46
6.2	Results	47
6.3	Discussion	48
6.3.1	Impact of supernova/host-galaxy mismatching on the Hubble diagram . .	48
6.3.2	Residuals of the MCMC fit	49
6.3.3	Implication on the late-time H_0 estimation	52
7	The impact of supernova blocking by the Milky Way on the estimation of H_0	54
7.1	Supernova sample selection	54
7.2	Results	55
7.2.1	General features of the $H_0(n\vec{G}_P)$ map	55
7.2.2	Galactic plane orientations of extrema H_0	56
7.3	Discussion	59
8	Conclusion	61
A	Extrema of the linear map described by a matrix	63

1 Introduction

1.1 The Hubble constant under tension

Standard cosmological parameters are the principal quantities through which we characterize the Universe. Determining these parameters, which are not directly predicted by a fundamental theory, is one of the central tasks of modern cosmology. Inferring cosmological parameters is a multidisciplinary exercise which relies on a combination of the theoretical framework provided by the assumed underlying cosmological model, observational data and statistical tools to confront the model with the data and extract the best fitting parameter values. Arguably, the most accessible parameter of the prevailing cosmological model (the cosmological constant cold dark matter (Λ CDM) model) is the Hubble constant (H_0), which quantifies the present-day expansion rate of the Universe.

The discovery of the expansion of the Universe and the first measurements of the Hubble constant in the early 20th century marked a pivotal moment in cosmology. In 1927, Georges Lemaître published a seminal paper in which he presented a formalism based on Einstein's equations that described an expanding Universe and coupled it with available observations of galaxies to suggest that they exhibited the distance-velocity relationship one might expect if the Universe was expanding [25]. Two years later, in 1929, Edwin Hubble made observations which revealed that all other galaxies appear to move away from us with a recession velocity which increases proportionally to their distance [22]. This relation, called the Hubble law, challenged the then-prevailing concept of a static Universe by providing compelling evidence of the expansion of the Universe. Upon this discovery, considerable effort was put to quantify the relationship between galaxy distances and recession velocities and to measure H_0 . Hubble's original estimation of H_0 was based on observations of Cepheid variable stars and yielded a value of ~ 500 km/s/Mpc [22], whereas nowadays the value of H_0 is believed to lie around ~ 70 km/s/Mpc. These early measurements were therefore affected by large uncertainties but they nevertheless paved the way for more precise and sophisticated measurements of H_0 in subsequent years.

Since Hubble's initial measurements, the methods for estimating the Hubble constant have undergone significant developments, incorporating more precise observational techniques and refined theoretical models. However, despite these improvements, accurately determining the Hubble constant remains, to this day, a complex and challenging task due to the intricate interplay between different cosmological observations and the need to account for many systematic uncertainties. Nowadays, two primary methods are used to estimate the Hubble constant. The first one is based on local measurements of the distances and redshifts (z) of supernovae in the late Universe. The second one is derived from measurements of the cosmological microwave background (CMB) in the early Universe.

In the late Universe, the leading method for measuring the Hubble constant is based on distance and redshift of Type Ia supernovae (SNe Ia). These types of supernovae produce, at their peak, a fairly constant luminosity allowing them to be used as “standard candles”. The distance to SNe Ia can be determined with very high precision by comparing this known intrinsic luminosity to the brightness of the source observed on Earth. The redshift of supernovae is typically determined by analysing the displacement of the spectral lines of their host-galaxy. Under the assumption of the Λ CDM model, the observed distance and redshift to a source are coupled through a H_0 -dependent relation. This relation can be exploited to infer a value for H_0 which fits our supernovae observations. The latest and most thorough of such measurements was carried out in the context of the SH0ES program (*Supernovae and H_0 for the Equation of State of dark energy*) as part of the *Pantheon+* analysis [8]. This latest SH0ES collaboration estimated the expansion rate in the local Universe based on 1550 unique, spectroscopically confirmed SNe Ia from 18 different surveys with redshifts ranging from $z = 0.001$ to $z = 2.26$. This constitutes the most complete SNe Ia catalogue available to date. This analysis yielded a value of $H_0 = 73.5 \pm 1.1$ km/s/Mpc [8].

The value of the Hubble constant can also be predicted from the early, pre-recombination Universe (corresponding to $z \geq 1100$). This is done, by measuring the angular power spectrum of the CMB temperature fluctuations. The observed angular spectrum of the CMB is characterized by peaks and troughs which are thought to be the consequence of acoustic waves in the baryon-photon fluid at the time of photon/matter decoupling. The exact locations, heights and depths of these peaks and troughs in the observed power spectrum are directly related to the mean density of the baryonic matter as well as other cosmological parameters including H_0 , allowing us to derive constraints on the Hubble constant through an alternative method. Extrapolating H_0 from CMB measurements can only be done under the assumption of a particular cosmological model which described the expansion history of the Universe (typically the Λ CDM model) such that this estimation is indirect and model-dependent. The “gold-standard” of these early Universe measurements was carried out by *Planck* in 2018 which led to a value for the Hubble constant of $H_0 = 67.27 \pm 0.60$ km/s/Mpc at 68% confidence level [30].

Both the early-time and the late-time estimation of H_0 rely on the assumption of the Λ CDM model, but the degree of model-dependence varies between the two methods. The early-time estimation of H_0 relies on the accuracy of certain assumptions of the Λ CDM model regarding the early Universe ($z \geq 1000$). In particular, some of these ansatzes concern neutrino properties, particle interactions, the absence of primordial magnetic fields and the scalar spectral index. Moreover, the Λ CDM model is then assumed to describe the evolutionary history of the Universe from $z = 1000$ onward in order to extrapolate the current expansion rate from the parameters derived in the early Universe. The late-time estimation of H_0 relies on different assumption inherent to the Λ CDM model such as the description of dark matter (as cold and non-interacting) and the representation of dark energy by a cosmological constant (Λ). Measurements of the Hubble constant in the local Universe are therefore often regarded as more empirical.

Comparing the value of H_0 measured locally to that predicted from the early Universe measurements is an essential “end-to-end test” of the validity of the currently accepted Λ CDM model over the largest possible time span: from the dense, dark-matter dominated, early Universe to the current, dilute, dark-energy dominated Universe.

In the last few decades, the advances in experimental sensitivity have allowed for increasingly refined measurements and improved data sets. Surprisingly, these improvements in the estimates of H_0 have led to the emergence of a persisting statistically significant discrepancy between the values obtained through these two different methods. Concretely, the discordance of the Hubble constant determined through early time and late time methods ranges from 4σ to 6σ depending on the specific data set used. This so-called “Hubble tension” is considered to be one of the most long-lasting and widely persisting challenges faced by contemporary cosmology [37]. The discrepancy between the two estimations is of the order of $\sim 10\%$ such that uncovering this tension has only been possible with the improved precision of recent cosmological surveys.

Despite providing the most precise constraints on the Hubble constant obtained to date, the estimates from the *Planck* angular spectra, like any experimental measurement, are not exempt from systematic errors. However, no source of systematic uncertainty has been found in these measurements which could increase the value of H_0 by more than 1 km/s/Mpc. Therefore, the Hubble tension could probably be alleviated with these systematic errors in the CMB measurements but they cannot fully explain the existing tension. It is also worth noting that percent-level precision in H_0 claimed in the *Planck* results is achieved at the expense of strong model assumptions. Moreover, the data reduction of the cosmological surveys used, which is performed before fitting the cosmological model, is often also performed in the context of the Λ CDM model. This means that analysing the measured power spectrum under the assumption of a different cosmological model could be one way to solve the Hubble tension [37].

Distance and redshift measurements of SNe Ia are not free of systematic uncertainties either. Despite various reanalyses of the SH0ES data employing different approaches, statistical inference methods, or modifications to the dataset, none of them has yielded a significant modification in H_0 . Additionally, a significant mismatch between early Universe and late Universe measurements of H_0 persists across different measurements in our local Universe which are not apparently affected by the same systematic uncertainties. The level of attention dedicated to these measurements is now such that any important source of systematic uncertainty should have been found [37]. It is therefore becoming increasingly unlikely that systematic uncertainties in either of the measurements can solely be responsible for the Hubble tension.

As shown in Fig. 1, there exist various alternative, independent approaches to estimate H_0 in addition to the commonly used methods involving SNe Ia and CMB measurements. Measurements based on gravitational lensing [39, 13, 6] and the Tully-Fisher relation [23, 34] align

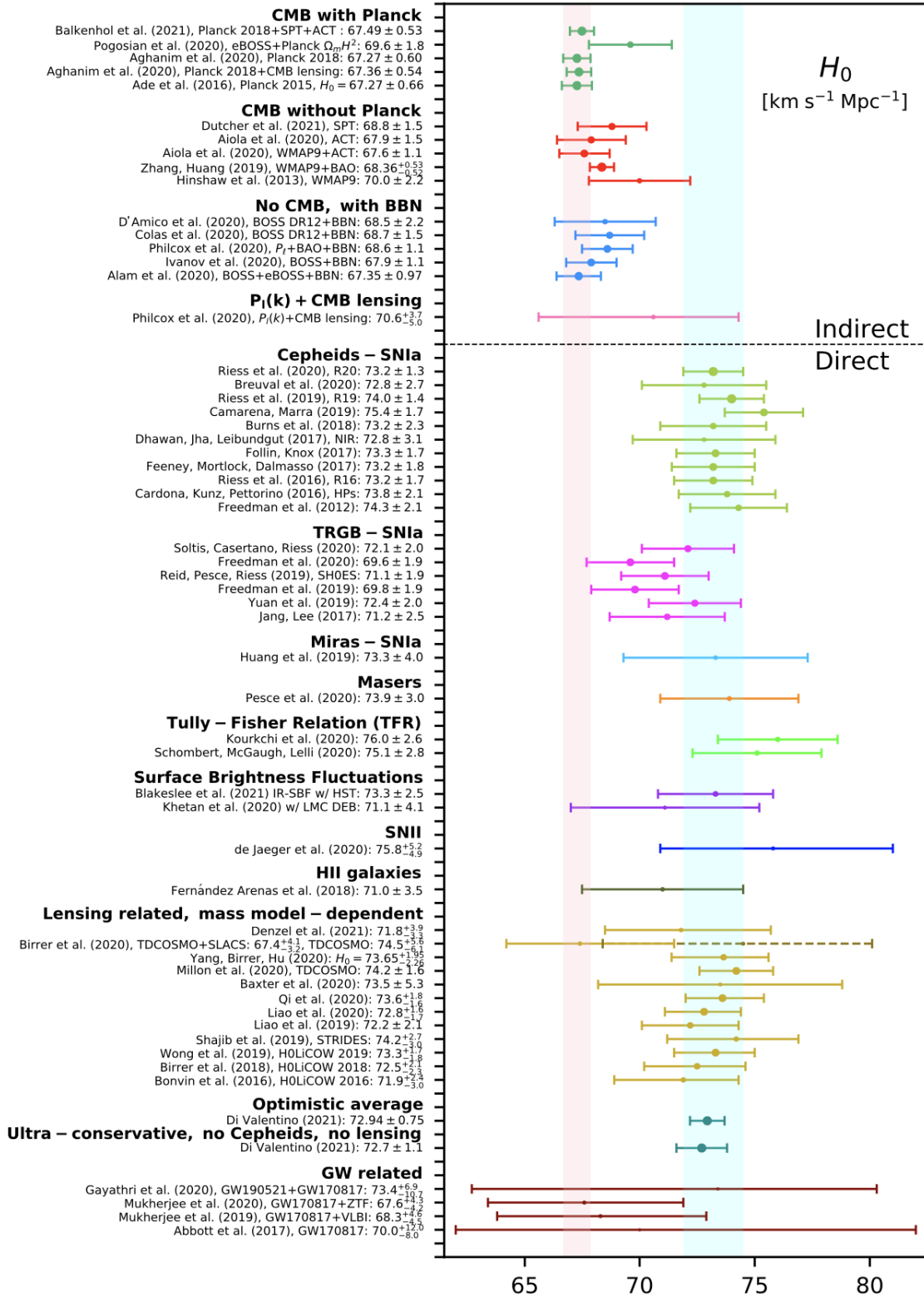


Figure 1: Whisker plot of the 68% confidence intervals of different measurements of H_0 performed over the last decade. These measurements are categorized into early-Universe measurements in the top part of the figure and late-Universe measurements in the bottom part of the figure. The cyan vertical band corresponds to the 68% confidence interval of H_0 from the SH0ES estimation [32] and the pink vertical band corresponds to the 68% confidence interval of H_0 from the Planck estimation [30]. (Source: [37])

with the local results obtained from supernovae observations while estimations derived from Big Bang nucleosynthesis [4] show consistency with the results obtained from the CMB. Upon consideration of these different methods, the Hubble tension seems to appear as a difference between the value of H_0 predicted from measurements in concert with early-Universe physics and that measured in the late Universe over a distance scale of ~ 400 Mpc.

The Λ CDM model is a simple and elegant framework which accounts for most of the cosmological data available to date. However, despite its great success so far, it relies on strong assumptions concerning dark matter, dark energy and inflation of which the underlying physics remains largely unknown to this day. In this context, the Hubble tension could be interpreted as a harbinger of new physics, indicating that the assumed Λ CDM model is failing (at least partially) in the early or in the late Universe. Various attempts to reconcile the discrepancy in H_0 by means of physics beyond the concordance Λ CDM model involve extended cosmological models incorporating new parameters in addition to those of the standard Λ CDM model. However, including extra free parameters often leads to broadened uncertainties on H_0 such that the attenuation of the Hubble constant is attributed to the increase of the error bars rather than an actual shift in the central value. As we currently do not have any other model to replace it with, many cosmologists are still reluctant to discard the Λ CDM model altogether. Therefore, it is still highly relevant to look for new sources of biases or errors in our measurements of H_0 in the local Universe which assume the Λ CDM model.

1.2 Research motivation

In this respect, the purpose of this research is to analyse the biases introduced in our late-time estimation of H_0 by the obstruction of certain SNe Ia by foreground galaxies in our observations. In total, we look at three different situations in which supernovae are obstructed by foreground galaxies in our observations and we estimate the impact on the estimation of H_0 in each of these cases.

1.2.1 Total blocking of supernovae by foreground galaxies

Estimating H_0 accurately from SNe Ia distance measurements requires extensive supernovae samples spanning the largest redshift range possible. To achieve this, the constraints on the Hubble constant are derived using a compilation of multiple different SNe Ia samples, each resulting from a survey optimized to observe sources in a different redshift range. At high redshift ($z \gtrsim 0.1$), SNe Ia are typically observed through deep pencil beam surveys such as [33]. At lower redshifts, where they are scarcer, SNe Ia are observed through full sky surveys such as the one presented in [16]. It can happen that in these observed samples, a supernova and a galaxy in its foreground lie on the same line-of-sight, such that from our perspective the light coming from the supernova is obstructed by the foreground galaxy. Depending on the absolute and relative distances of the two objects as well as the properties of the galaxy, this can lead to two different “blocking scenarios” which each bias our estimation of H_0 in a different way.

In the first case, the light emitted by the supernova can be completely overpowered by that of the foreground galaxy such that the supernova will no longer be visible to us. This would be the case if the relative distance between the obstructed supernova and the foreground galaxy is large, the foreground galaxy is very bright or the alignment between both objects is such that the supernova lies behind the bulge of a spiral galaxy. This “total blocking” is the most extreme of the supernova obstruction scenarios. The first bias on H_0 that we estimate in this research is the selection bias induced by this total blocking on our observed SNe Ia samples.

1.2.2 Supernova/host-galaxy mismatching

In the second scenario, the light emitted by the supernova can still be visible to us through the foreground galaxy. This can be the case if the relative distance between the two objects is small, the alignment between the supernova and the centre of the galaxy is less exact or the galaxy is less bright. This second scenario leads to a different type of bias on our estimation of the Hubble constant related to the currently preferred method to measure the redshift of supernovae. The estimation of the H_0 is based on comparing their measured distances to those expected from their measured redshifts, under the assumption of a FLRW metric. Therefore, the value of this method greatly relies on our ability to accurately measure SNe Ia redshifts. The preferred approach is to measure them indirectly through the spectroscopic redshift of their host-galaxy. This leads to a higher accuracy and precision because galaxies have sharper spectral lines than supernovae. An essential and non-trivial task is therefore to correctly match each supernova to its host-galaxy [9]. In the absence of spectroscopic information on the supernova, host-galaxy/supernova matching is done by looking at all the galaxies in a radius of $\sim 30''$ around each supernova and selecting the one for which the angular separation between the galaxy and the supernova, normalised by the elliptical radius of the galaxy in the direction of the supernova, is minimized [20]. This method is not impervious to mistakes when it comes to obstructed supernovae which have a very small angular separation to the foreground galaxy obstructing them. These supernovae could therefore be incorrectly matched to their obstructing galaxy instead of their true host-galaxy. This would cause their redshifts to be systematically underestimated, therefore biasing our estimation of H_0 . This is the second bias on H_0 caused by supernova obstruction that we evaluate in this research.

1.2.3 Supernova blocking by the Milky Way

Finally, the Milky Way also obstructs the supernovae in certain regions of the sky. Part of the sky is blocked by the Milky Way’s disk, leading to an empty gap in our observations. The supernovae lying behind the Milky Way’s disk can therefore not be observed, introducing a selection bias in our SNe Ia samples. Specifically which SNe Ia are missing from our observations depends on the orientation of the Milky Way’s disk. We therefore look at the impact of the Milky Way’s orientation on the estimated value of H_0 .

The remainder of this thesis is structured as follows: Section 2 provides an overview of the theoretical cosmology framework on which this work is based. The method employed to estimate the Hubble constant from a sample of SNe Ia is discussed in Section 3. In Section 4, we explain how the catalogue of simulated galaxies and SNe Ia, used for this analysis, is constructed and present the statistics of supernova blocking within this catalogue. Section 5 is dedicated to determining and discussing the impact of the selection bias caused by the “total blocking” of certain supernovae on the estimation of H_0 . In Section 6, we assess the impact of mistaking the obstructing galaxy with the host-galaxy of obstructed supernovae on the estimation of H_0 . Finally, in Section 7 we evaluate the impact of the orientation of the Milky Way’s plane on the estimation of H_0 before concluding in Section 8.

2 Theoretical cosmology framework

This section is dedicated to briefly covering the most important concepts of cosmology which make up the theoretical framework for the present research work. This section is mainly based on [14], [38], [26] and [40].

2.1 The homogeneous and isotropic Universe

In general relativity, the Einstein equations relate the geometry of spacetime (described by the Einstein tensor $G_{\mu\nu}$) to the distribution of the matter and energy it contains (described by the energy-momentum tensor $T_{\mu\nu}$). The Einstein equations are a set of ten non-linear second-order partial differential equations, representing the components of the metric tensor, which can be summarized in the following tensor equation

$$G_{\mu\nu} + \Lambda g_{\mu\nu} = 8\pi G T_{\mu\nu}. \quad (1)$$

In this equation, $G_{\mu\nu}$ is the Einstein tensor, Λ is the cosmological constant, $g_{\mu\nu}$ is the spacetime metric, G is Newton's gravitational constant and $T_{\mu\nu}$ is the energy-momentum tensor.

The Einstein tensor is defined in terms of the Ricci tensor $R_{\mu\nu}$, which depends on the metric and its derivatives, and the Ricci scalar \mathcal{R} , which is a contraction of the Ricci tensor ($\mathcal{R} = g^{\mu\nu} R_{\mu\nu}$) such that

$$G_{\mu\nu} = R_{\mu\nu} - \frac{1}{2} g_{\mu\nu} \mathcal{R}. \quad (2)$$

Therefore, the left-hand side of the Einstein equation is a function of the metric describing spacetime and the right-hand side depends on the constituents of the Universe. These equations state that the geometry of spacetime is a consequence of the presence and distribution of matter and energy.

Exact solutions to the Einstein equation can only be found under the assumption of some simplifications. The most straightforward simplifying assumption is the cosmological principle, which states that, on sufficiently large scales, the Universe can be considered spatially homogeneous and isotropic. This postulate is based on the assumption that neither the laws of physics nor the events in nature should appear differently to different observers. In this respect, the cosmological principle can be regarded as a generalisation of the Copernican principle according to which our location in the Universe should not, in any way, be a privileged one.

Such a spatially homogeneous and isotropic Universe can be described by the Friedmann-Lemaître-Robertson-Walker (FLRW) metric $\bar{g}_{\mu\nu}$, given by the line element

$$ds^2 = \bar{g}_{\mu\nu} dx^\mu dx^\nu = -dt^2 + a^2(t) \left[\frac{dr^2}{1 - kr^2} + r^2(d\theta^2 + \sin^2\theta d\phi^2) \right]. \quad (3)$$

In this line element, $a(t)$ corresponds to the dimensionless cosmic scale factor and k is the curvature scalar. The scale factor is a mathematical quantity which describes how the proper distance between two points changes as the Universe expands. It is defined relative to the present-day scale factor such that $a_0 = a(t_0) = 1$ and it is related to the redshift through $a(t) = a_0/(1+z) = 1/(1+z)$. The curvature scalar, which characterizes the curvature of space-time, is positive ($k > 0$) for a closed Universe, negative ($k < 0$) for an open Universe and null ($k = 0$) for a flat, Euclidean Universe.

The expansion of the Universe is measured through the time-dependent Hubble parameter which is defined in terms of the scale factor as

$$H(t) \equiv \frac{\dot{a}(t)}{a(t)}, \quad (4)$$

where $\dot{a}(t)$ corresponds to the time derivative of the scale factor. The Hubble parameter at $t = t_0$ corresponds to the Hubble constant H_0 .

Likewise, the cosmological principle constrains the form of the energy-momentum tensor. In order for $T_{\mu\nu}$ to reflect the homogeneity and isotropy of the Universe it must take the form of a perfect fluid

$$T_{\mu\nu} = (\rho + P)u_\mu u_\nu + P\eta_{\mu\nu}, \quad (5)$$

where ρ and P are the density and the pressure of the fluid, u_μ is its four-velocity with respect to the observer and $\eta_{\mu\nu}$ is the diagonal metric $\eta_{\mu\nu} = \text{diag}(-1, 1, 1, 1)$. (In an isotropic Universe, the space components of the four-velocity must be 0 such that $u_\mu = (-1, 0, 0, 0)$.)

Therefore, under the assumption of the cosmological principle, the energy-momentum tensor is diagonal and depends only on density and pressure. The total energy-momentum tensor is a sum of the energy-momentum tensors of each of the components of the Universe: baryonic matter, dark matter, radiation (photons and relativistic neutrinos) and dark energy.

In a homogeneous and isotropic Universe, where the metric takes the form of Eq. 3 and the energy-momentum tensor is given by Eq. 5, the Einstein equations simplify to the Friedmann equations

$$H^2 = \left(\frac{\dot{a}}{a}\right)^2 = \frac{8\pi G}{3}\rho - \frac{k}{a^2} + \frac{\Lambda}{3}, \quad (6a)$$

$$H^2 + \dot{H} = \frac{\ddot{a}}{a} = -\frac{4\pi G}{3}(\rho + 3P) + \frac{\Lambda}{3}. \quad (6b)$$

The first Friedmann equation (Eq. 6a) follows from the time-time component of the Einstein equations while the second Friedmann equation (Eq. 6b) follows from the space-space components of the Einstein equations.

The curvature of the Universe can be determined by comparing its energy density to the critical density ρ_c of a flat Universe which is defined, in terms of the Hubble parameter, as

$$\rho_c(t) \equiv \frac{3H(t)^2}{8\pi G}. \quad (7)$$

It is therefore conventional to express the present-day density $\rho_x(t_0)$ of the different components of the Universe in terms of the present-day critical density $\rho_c(t_0)$ by defining the following density parameters

$$\Omega_x \equiv \frac{\rho_x(t_0)}{\rho_c(t_0)} = \frac{8\pi G}{3H_0^2} \rho_x(t_0), \quad (8)$$

where the subscript x is either b for baryonic matter, r for radiation, DM for dark matter or Λ for dark energy. For dark energy, the cosmological constant is related to the dark energy density through $8\pi G\rho_\Lambda(t) = \Lambda$ such that $\Omega_\Lambda = \Lambda/3H_0^2$.

In addition, the curvature density parameter is given by

$$\Omega_k = \frac{-k}{H(t)^2 a(t)^2}. \quad (9)$$

By expressing the first Friedmann equation at time t_0 in terms of the density parameters, it follows that the densities of the different constituents of the Universe are related to each other by

$$\Omega_b + \Omega_r + \Omega_{\text{DM}} + \Omega_k + \Omega_\Lambda = 1. \quad (10)$$

The first Friedmann equation may also be written at any time as

$$H(z)^2 = \left(\frac{\dot{a}}{a}\right)^2 = \left(\frac{\dot{z}}{1+z}\right)^2 = H_0^2 \left[\Omega_r(1+z)^4 + \Omega_b(1+z)^3 + \Omega_{\text{DM}}(1+z)^3 + \Omega_k(1+z)^2 + \Omega_\Lambda \right]. \quad (11)$$

This form of the Friedmann equation relates the evolution of the Hubble parameter to the evolution of the density parameters and will later prove itself to be very useful to define distance measures in an expanding universe.

2.2 Large-scale inhomogeneities

In reality, the Universe is neither homogeneous nor isotropic on all scales. As evidenced by maps of the galaxy distribution in the local Universe such as the one in Fig. 2 resulting from the Sloan Digital Sky Survey (SDSS), the Universe exhibits structure on large scales. This structure takes the form of a web-like pattern where galaxies clump together in galaxy clusters and superclusters along filamentary structures separated by vast regions in between. However, overall statistical properties of the Universe, when observed on sufficiently large scales, nonetheless present a high degree of homogeneity and isotropy.

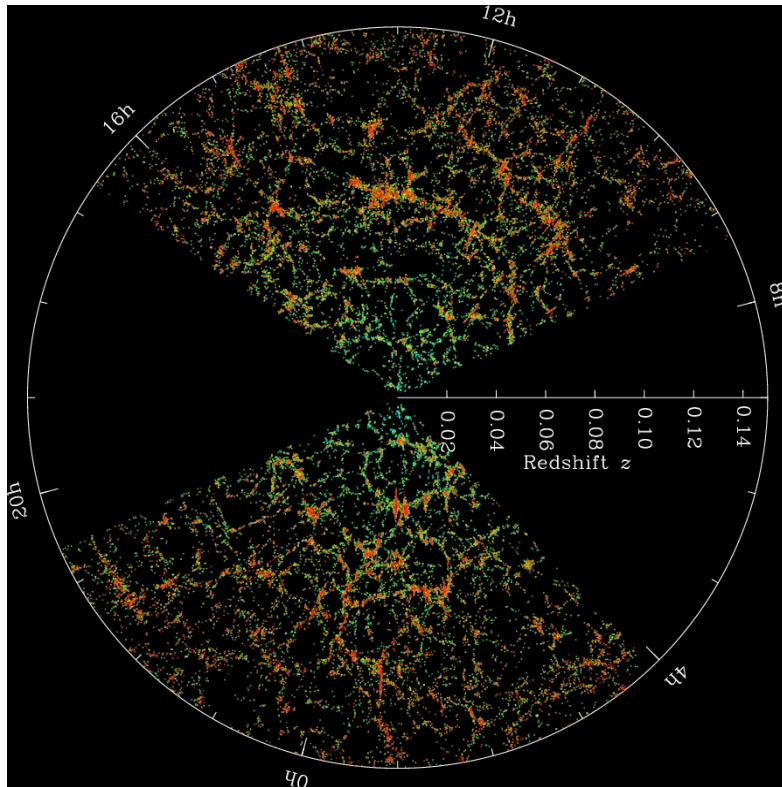


Figure 2: Slice of the 3-dimensional map of the distribution of galaxies in the local Universe. Each point on this map represents a galaxy, which is coloured according to the age of the stars it contains with redder galaxies containing older stars. The Earth is located at the centre of the map and the outer circle represents a radius of two billion light years. The empty wedges could not be mapped because dust in our own Milky Way obscures the view of the distant universe in these directions. *Credits: M. Blanton and the Sloan Digital Sky Survey*

These inhomogeneities in the matter density field are therefore treated as linear order perturbations around the background FLRW spacetime.

2.2.1 The FLRW metric and its perturbations

The metric describing this perturbed spacetime can then be expressed in terms of the FLRW metric $\bar{g}_{\mu\nu}$ and the (symmetric) perturbation metric $\delta g_{\mu\nu}$ as

$$g_{\mu\nu} = \bar{g}_{\mu\nu} + \delta g_{\mu\nu}. \quad (12)$$

The perturbations described by $\delta g_{\mu\nu}$ are assumed to be small, such that we require that the first derivative $\partial_\rho \delta g_{\mu\nu}$ and the second derivative $\partial_{\rho\sigma} \delta g_{\mu\nu}$ of the perturbation metric are small. The FLRW metric only depends on time whereas $\delta g_{\mu\nu}$ is both time- and space-dependent. This decomposition into a background metric and a perturbation is such that the spatial average of the perturbation term vanishes: the average of $g_{\mu\nu}$ over a slice of constant time t is equal to the value of $\bar{g}_{\mu\nu}$ at time t .

Using the definition of $\bar{g}_{\mu\nu}$ from Eq. 3, the components of the perturbed metric can be written as

$$g_{00} = \bar{g}_{00} + \delta g_{00} = -1 + \delta g_{00} \quad (13a)$$

$$g_{0i} = a^2(t)[\bar{g}_{0i} + \delta g_{0i}] = a^2(t)\delta g_{0i} \quad (13b)$$

$$g_{ij} = a^2(t)[\bar{g}_{ij} + \delta g_{ij}], \quad (13c)$$

where the Latin indices i and j run over the spatial components only and δg_{00} , δg_{0i} and δg_{ij} are the metric perturbations which depend both on time and space.

Assuming a flat ($k = 0$) FLRW metric, we can choose a coordinate system in which the spatial components of the background metric are given by

$$\bar{g}_{ij} = \eta_{ij}, \quad (14)$$

where η_{ij} is the three-dimensional metric tensor describing a flat 3-dimensional Euclidean space given by the diagonal elements $\eta_{ij} = \text{diag}(1, 1, 1)$.

Given the spatial symmetries of our observable Universe, the only type of transformation under which this requirement is fulfilled are rotations. For this reason, we classify the components of $\delta g_{\mu\nu}$ into scalar, vector and tensor components based on their behaviour under spatial rotations.

- The time-time component δg_{00} has no spatial index such that it remains invariant under spatial rotations. It therefore transforms like a scalar and can be written as $\delta g_{00} = -2A(t, \vec{x})$, where $A(t, \vec{x})$ is a scalar field. (The factor 2 and the sign are simply a matter of convention.)
- The time-space components δg_{i0} transform as the components of a 3-vector under spatial rotations such that we define $\delta g_{i0} = B_i$, where $\vec{B}(t, \vec{x})$ is vector field. Using the Helmholtz decomposition, $\vec{B}(t, \vec{x})$ can further be decomposed into a curl-free and a divergence-free part as

$$\vec{B} = \vec{B}^{(S)} + \vec{B}^{(V)}, \quad (15)$$

where $\nabla \times \vec{B}^{(S)} = 0$ and $\nabla \cdot \vec{B}^{(V)} = 0$. The gradient field $\vec{B}^{(S)}$ can then be expressed as the gradient of a scalar field $\beta(t, \vec{x})$ such that

$$\vec{B}^{(S)} = -\nabla\beta(t, \vec{x}). \quad (16)$$

The time-space component of the perturbation metric can therefore be written as

$$\delta g_{i0} = B_i = -\partial_i\beta(t, \vec{x}) - B_i^{(V)}(t, \vec{x}). \quad (17)$$

- The space-space components δg_{ij} transform as the components of a 3-tensor under rotations such that we define $\delta g_{ij} = 2C_{ij}$, where $C(t, \vec{x})$ is a tensor field. (The factor 2 is,

again, a matter of convention.) The tensor field $C(t, \vec{x})$ can firstly be decomposed into its trace-part and its traceless-part as

$$C_{ij} = \phi \bar{g}_{ij} + E_{ij}, \quad (18)$$

where $\phi(t, \vec{x})$ is a scalar field and E_{ij} is a symmetric traceless tensor field. The traceless part of C_{ij} can further be decomposed as

$$E_{ij} = E_{ij}^{(S)} + E_{ij}^{(V)} + E_{ij}^{(T)} \quad (19)$$

A symmetric tensor field can be generated by taking two spatial derivatives of a scalar field or by taking the derivative of a vector field with zero divergence such that we can rewrite

$$E_{ij}^{(S)} = (\partial_i \partial_j - \frac{1}{3} \delta_{ij} \nabla^2) \gamma = \partial_{\langle i} \partial_{j \rangle} \gamma \quad (20a)$$

$$E_{ij}^{(V)} = \partial_j C_i^{(V)} + \partial_i C_j^{(V)} = C_{(i|j)}^{(V)}, \quad (20b)$$

where $\gamma(t, \vec{x})$ is a scalar field and $C^{(V)}(t, \vec{x})$ is a vector field with $\nabla \cdot C^{(V)} = 0$. The last term $E_{ij}^{(T)}$ cannot be rewritten through derivatives acting on scalar or vector fields.

In total, the space-space component of the perturbation metric can therefore be written as

$$\delta g_{ij} = 2C_{ij} = 2 \left[\phi \bar{g}_{ij} + \partial_{\langle i} \partial_{j \rangle} \gamma + C_{(i|j)}^{(V)} + E_{ij}^{(T)} \right]. \quad (21)$$

The perturbation metric $\delta g_{\mu\nu}$ can therefore be decomposed into a scalar part consisting of $A(t, \vec{x})$, $\beta(t, \vec{x})$, $\phi(t, \vec{x})$ and $\gamma(t, \vec{x})$, a vector part consisting $B_i^{(V)}$ and $C_i^{(V)}$ and a tensor part consisting of $E_{ij}^{(T)}$.

The Einstein tensor $G_{\mu\nu}$ is defined in terms of the metric $g_{\mu\nu}$ and its derivatives. Therefore, in an inhomogeneous and anisotropic Universe, perturbations in the metric translate into perturbations in the Einstein tensor which can be decomposed as

$$G_{\mu\nu} = \bar{G}_{\mu\nu} + \delta G_{\mu\nu}, \quad (22)$$

where $\bar{G}_{\mu\nu}$ corresponds to the Einstein tensor in a homogeneous and isotropic Universe defined in terms of $\bar{g}_{\mu\nu}$ and its derivatives, while $\delta G_{\mu\nu}$ represents the perturbation part, defined in terms of $\delta g_{\mu\nu}$ and its derivatives. It is therefore possible to also decompose $\delta G_{\mu\nu}$ into scalar, vector and tensor components, such that the scalar perturbations in $\delta g_{\mu\nu}$ give rise to the scalar part of $\delta G_{\mu\nu}$, the vector perturbations in $\delta g_{\mu\nu}$ give rise to the vector part of $\delta G_{\mu\nu}$ and the tensor perturbations in $\delta g_{\mu\nu}$ give rise to the tensor part of $\delta G_{\mu\nu}$.

2.2.2 The energy-momentum tensor and its perturbations

Since the matter content of the Universe is related to the geometry of spacetime through the Einstein equations, perturbations in the metric also invoke perturbations in the energy-momentum tensor $T_{\mu\nu}$. In an inhomogeneous and anisotropic Universe, the energy momentum takes the form

$$T_{\nu}^{\mu} = (\rho + P)u^{\mu}u_{\nu} + P\delta_{\nu}^{\mu} + \Pi_{\nu}^{\mu}. \quad (23)$$

In this expression, ρ and P are the density and the pressure of the fluid, u^{μ} is its four-velocity with respect to the observer, Π_{ν}^{μ} is the anisotropic stress tensor and δ_{ν}^{μ} is the Kronecker delta tensor. The anisotropic stress tensor describes the stress and pressure gradients that arise from the anisotropy of the Universe. Unlike the isotropic pressure P , which is equal in all spatial directions, Π_{ν}^{μ} also has non-zero off-diagonal components that are direction-dependent.

These fluid quantities can be decomposed into the background quantities and the perturbations as

$$\rho = \bar{\rho} + \delta\rho \quad (24a)$$

$$P = \bar{P} + \delta P \quad (24b)$$

$$u^{\mu} = \bar{u}^{\mu} + \delta u^{\mu}, \quad (24c)$$

where $\bar{\rho}$, \bar{P} and \bar{u}^{μ} correspond to the quantities in the background Universe and $\delta\rho$, δP and δu^{μ} correspond to the perturbations. For convenience, we rewrite the velocity perturbation as $u^{\mu} = (\bar{u}^0 + \delta u^0, \delta u^1, \delta u^2, \delta u^3) = (\bar{u}^0 + \delta u^0, v_i)$.

The energy momentum tensor can then also be decomposed into the background energy-momentum tensor \bar{T}_{ν}^{μ} and the energy-momentum perturbation tensor δT_{ν}^{μ} in the same way

$$T_{\nu}^{\mu} = \bar{T}_{\nu}^{\mu} + \delta T_{\nu}^{\mu}, \quad (25)$$

where the energy-momentum perturbation is built out of the scalar perturbations $\delta\rho(t, \vec{x})$ and $\delta P(t, \vec{x})$, the vector field $\vec{v}(t, \vec{x})$ and the traceless 3-tensor Π_{ij} .

Applying the same procedure used previously to decompose the perturbations in the metric, the velocity vector field \vec{v} can be decomposed as

$$\vec{v} = \vec{v}^{(S)} + \vec{v}^{(V)}, \quad (26)$$

where $\nabla \times \vec{v}^{(S)} = 0$ and $\nabla \cdot \vec{v}^{(V)} = 0$. We can therefore rewrite $\vec{v}^{(S)} = -\nabla v(t, \vec{x})$.

In the same way, we also split the traceless anisotropic stress tensor Π_{ij} as

$$\Pi_{ij} = \Pi_{ij}^{(S)} + \Pi_{ij}^{(V)} + \Pi_{ij}^{(T)}, \quad (27)$$

which allows us to rewrite $\Pi_{ij}^{(S)}$ in terms of a scalar field $\pi(t, \vec{x})$ and $\Pi_{ij}^{(V)}$ in terms of a vector field $\vec{S}(t, \vec{x})$ as

$$\Pi_{ij}^{(S)} = (\partial_i \partial_j - \frac{1}{3} \delta_{ij} \nabla^2) \pi = \partial_{(i} \partial_{j)} \pi \quad (28a)$$

$$\Pi_{ij}^{(V)} = \partial_j S_i^{(V)} + \partial_i S_j^{(V)} = S_{(i|j)}^{(V)}. \quad (28b)$$

The energy-momentum perturbation tensor δT_{ν}^{μ} can therefore be decomposed into a scalar part consisting of $\delta\rho(t, \vec{x})$, $\delta P(t, \vec{x})$, $v(t, \vec{x})$ and $\pi(t, \vec{x})$, a vector part consisting of $v_i^{(V)}$ and $S_i^{(V)}$ and a tensor part consisting of $\Pi_{ij}^{(T)}$.

The large-scale structure that we observe in the Universe is caused by the scalar perturbations in the metric which couple to the density and pressure perturbations in the energy-momentum tensor. Vector perturbations introduce an additional layer of complexity, as they are associated with rotational motions and flows in the matter distribution such as the peculiar motions of galaxies. However, vector perturbations decay in an expanding Universe and can therefore often be ignored. Tensor perturbations are associated with the generation of gravitational waves and their propagation through spacetime. As stated by the decomposition theorem, these three different types of perturbations evolve independently at linear order. Vector and tensor perturbations can therefore be neglected when trying to understand the origin and evolution of the Universe's large-scale structure.

In the context of the late-time estimation of the Hubble constant, these large-scale inhomogeneities mainly come into play in the form of gravitational lensing and peculiar velocities. The way in which these two effects affect the inference of H_0 is discussed in more detail in section 3.1.1 and section 3.1.2.

2.3 The Λ CDM model

The Λ -Cold Dark Matter (Λ CDM) model is the simplest cosmological model parametrisation which accounts for most of the cosmological data available to date and is therefore often referred to as the “standard model” of contemporary cosmology. The Λ CDM model rests on the foundational assumptions that the Universe is homogeneous and isotropic on large scales as well as flat and in accelerated expansion. The geometry of the Universe can therefore be described by the FLRW metric (Eq. 3) with $k = 0$. While these assumptions are not specific to the Λ CDM model, the Λ CDM model is additionally characterized by the theory of inflation and the abundance of dark matter and dark energy.

2.3.1 Inflation

The first pillar of the Λ CDM model is the theory of inflation which explains how primordial quantum fluctuations became the seeds for the large-scale structure we observe today. Inflation suggests that during a brief epoch in the very early Universe, the scale factor grew exponentially.

During this time, the Universe was expanded by a factor of at least 10^{26} causing the primordial density fluctuations to blow up to large scales. This inflationary epoch is believed to have taken place $\sim 10^{-32}$ s after the Big Bang and would have lasted 10^{-35} s. The simplest mechanism to drive such an exponential expansion is via the potential energy of a scalar field (the inflation). However, as of today, there is no known scalar field that can drive inflation. In addition, the theory of inflation predicts that the statistical distribution from which these primordial quantum perturbations are drawn is Gaussian and almost scale-invariant. The fundamental physics on which inflation is based might only manifest itself on energy scales which exceed our experimental capability, making it very difficult to verify this theory. However, its predictions on the distribution of primordial quantum fluctuations have been verified through the observations of the Cosmic Microwave Background (CMB) carried out in the context of the *Planck* mission [29], which is considered an important confirmation of the theory of inflation.

2.3.2 Composition of the Universe

Additionally, the Λ CDM model relies on the assumption that dark energy and (cold) dark matter are the dominant components of the Universe. The most popular theory concerning dark matter nowadays describes it as consisting of relics of elementary particles from the early Universe. Although the exact nature of dark matter particles remains unknown, we hypothesise that dark matter particles must be “cold”. This means that their velocity must be below the one of photons at the epoch of radiation-matter equality. This requirement ensures that dark matter particles are able to clump together efficiently in the early stages of the Universe to later give rise to the structures observed today. In addition to being cold, dark matter is also assumed to be non-dissipative (it cannot cool down by radiating photons) and collisionless (dark matter particles interact only through gravitational interactions and possibly the weak force) dark matter accounts for about 26.5 % of the total mass-energy density of the Universe [36].

Dark energy, which is represented by the cosmological constant Λ in the Einstein field equations (Eq. 1), is currently the preferred explanation of the observed accelerated expansion of the Universe against the attractive effects of gravity. In comparison to the other forms of energy present in the Universe, this vacuum energy density has the particularity of remaining constant through time and space despite the expansion of the Universe, thus acting as a cosmological constant. Dark energy is believed to be the dominant component of our present-day observable Universe: according to the latest *Planck* measurements of the CMB anisotropies, dark energy accounts for 68% of the total energy [30].

To a lesser extent, the Universe also contains baryonic matter (which accounts for about 5% of the content of the Universe [36]) and an almost negligible fraction of radiation. The density of baryonic matter and that of dark matter are often considered together in the total matter density parameter $\Omega_m = \Omega_b + \Omega_{\text{CDM}}$. Moreover, the density of radiation is often assumed to be negligible ($\Omega_r \simeq 0$) and the Universe is assumed to be flat ($\Omega_k = 0$) such that we are left

only with two density parameters Ω_m and Ω_Λ . Since, the sum of the density parameters of all components must be unity (Eq. 10) we rewrite $\Omega_\Lambda = 1 - \Omega_m$. Under these assumptions and simplifications, the present-day content of the Universe can therefore be parameterized in terms of the total matter density Ω_m and the Hubble constant H_0 only. In addition to the Hubble constant and the different density parameters, the Λ CDM model is constrained by other cosmological parameters related to the history of the early Universe including the density perturbation spectral index, the tensor-to-scalar perturbation ratio and the ionisation optical depth. However, as these other parameters are not relevant to this research they will not be discussed in more detail.

2.4 Distance measures in cosmology

2.4.1 Theoretically-defined distances

In an expanding Universe, the distance between two events is not uniquely defined: different definitions of distance are appropriate for different applications. These different definitions are all asymptotic for small redshifts ($z \ll 1$) but they diverge noticeably beyond $z \sim 1$ (see Fig. 3). The unifying factor of all definitions is that they all quantify the separation between events of photon trajectories which end at the observer (radial null geodesics of spacetime).

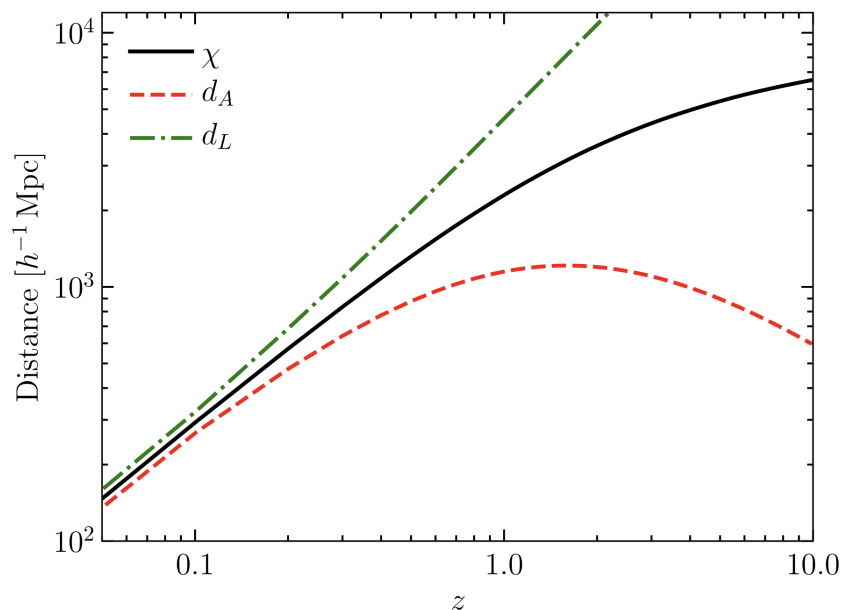


Figure 3: Three alternative distance measures in an expanding Universe as a function of redshift: the comoving distance $\chi(z)$, the angular diameter distance $d_A(z)$ and the luminosity distance $d_L(z)$. *Source:*[14]

The comoving distance The starting point for all cosmological distance measures is the comoving distance χ . The comoving distance between two comoving observers (both moving with the Hubble flow) remains constant through time, despite the expansion of the Universe, as

the comoving coordinates it is expressed in take this expansion into account.

When written in the form of Eq. 3, the FLRW metric places all the time-dependence into the scale factor $a(t)$ such that the coordinates r, θ, ϕ are time-independent. Therefore, any distance expressed only in terms of these coordinates is a comoving distance. Starting from the FLRW metric, for a photon moving on a radial, null geodesic we have that $d\theta = d\phi = 0$ and $ds^2 = 0$, such that the line element may be written as

$$-dt^2 + a^2(t) \frac{dr^2}{1 - kr^2} = 0. \quad (29)$$

In a small time interval dt , light emitted by a source therefore travels a comoving distance given by

$$d\chi = \frac{dt}{a(t)} = \frac{dr}{\sqrt{1 - kr^2}}. \quad (30)$$

The comoving distance between a light source at coordinate distance r and an observer at $r = 0$ is then given by

$$\chi = \int_0^\chi d\chi' = \int_t^0 \frac{dt'}{a(t')} = \int_r^0 \frac{dr'}{\sqrt{1 - kr'^2}}. \quad (31)$$

This integral has the three following solutions depending on the curvature of the Universe

$$\chi(r) = \begin{cases} \frac{1}{\sqrt{|k|}} \sinh^{-1} \sqrt{|k|r} & k < 0 \\ r & k = 0 \\ \frac{1}{\sqrt{k}} \sin^{-1} \sqrt{kr} & k > 0. \end{cases} \quad (32)$$

Therefore, in a flat Universe, the comoving distance χ coincides with the coordinate distance r , which is not the case in a non-flat Universe.

Alternatively, the comoving distance can also be written as

$$\chi = \int_t^0 \frac{dt'}{a(t')} = \int_{a(t)}^1 \frac{da'}{a'^2 H(a')} = \int_0^z \frac{dz'}{H(z')}, \quad (33)$$

where we first change the variable of integration from t' to a' , which introduces the additional factor $\dot{a} = aH$ in the denominator, and then from a' to z' in the second step.

Using the expression for $H(z)$ introduced previously from the Friedmann equation (Eq. 11), the comoving distance may then be rewritten as

$$\chi(z) = \frac{1}{H_0} \int_0^z \frac{dz'}{\sqrt{\Omega_r(1+z')^4 + \Omega_m(1+z')^3 + \Omega_k(1+z')^2 + \Omega_\Lambda}}. \quad (34)$$

In this form, it becomes apparent that the comoving distance is a model-dependent quantity which relies on the density parameters assumed for the different components of the Universe. The comoving distance can be considered as the “fundamental” distance measure in cosmology since, as we will see now, all other definitions of distance can be written in terms of the comoving distance.

The proper distance The proper distance between two events α and β is the distance that separates them in a reference frame where they take place simultaneously (such that $t_\alpha = t_\beta$). The proper distance $d_P(t)$ between two events separated by a comoving distance χ is given by

$$d_P(t) = a(t) \cdot \chi. \quad (35)$$

While the comoving distance remains constant, the proper distance changes over time due to the expansion of the universe. The comoving distance and proper distance between two events is therefore only equal at the present time where $a(t_0) = 1$.

An important caveat of these two definitions of distance is that they are both derived theoretically from the Λ CDM model and its fitted parameters but neither of them can be measured experimentally. As mentioned previously, the late-time estimation of H_0 relies greatly on our ability to measure the distance of supernovae. Therefore, we will now discuss two additional definitions of distance which are defined both theoretically from the Λ CDM model and experimentally through observable quantities.

2.4.2 Observable distances

The angular diameter distance A common way of determining the distance to faraway sources is by means of the angular diameter distance d_A . The angular diameter distance to a source is found by comparing the known physical size l of a source and the measured angle it subtends on the sky $\delta\theta$. (Such objects of known physical sizes are called “standard rulers”.) For distant sources we can make use of the small angle approximation such that, from an observational point of view, the angular diameter distance is defined as

$$d_A = \frac{l}{\delta\theta}. \quad (36)$$

In an expanding Universe, the angle subtended on the sky by a source of physical size l is generalized to account for the effect of cosmic expansion. Suppose that the source emits light at time $z = z_e$ which is received by an observer located at a comoving distance $\chi(z_e)$ from the source. From the point of view of the observer, the angle subtended by the source on the sky is then given by

$$\delta\theta = \frac{l}{a(z_e)\chi(z_e)}. \quad (37)$$

Therefore, relating Eq. 36 and Eq. 37 we find that, the angular diameter distance is defined alternatively in terms of the comoving distance as

$$d_A = a(z_e) \cdot \chi(z_e). \quad (38)$$

Substituting the definition for the comoving distance as a function of redshift introduced previously (Eq. 33) and using $a(z) = 1/(1+z)$ we find that, from a theoretical point of view, the angular diameter distance is given by

$$d_A(z) = \frac{1}{(1+z)H_0} \int_0^z \frac{dz'}{\sqrt{\Omega_r(1+z)^4 + \Omega_m(1+z')^3 + \Omega_k(1+z)^2 + \Omega_\Lambda}}. \quad (39)$$

As shown in Fig. 3, the angular diameter distance $d_A(z)$ is not a monotonically increasing function, as one could expect, but has a turnover point at $z_T \sim 1$ instead. Referring back to Eq. 36, this means that an object of physical size l spans an increasingly small angle on the sky until $z = z_T$ where $\delta\theta$ is minimal but beyond z_T it will span an increasingly larger angle as z increases. This counter-intuitive effect is a consequence of the expansion of the Universe in combination with the finite speed of light.

Two “competing” effects determine the size of the angle subtended by a source on the sky. On one hand, we intuitively expect distant objects to span increasingly small angles on the sky. On the other hand, because the Universe is expanding while light travels at a finite speed, it is important to distinguish the angle $\delta\theta_E$ spanned by the source when the light was emitted at time t_E from the angle $\delta\theta_R$ that the source spans upon reception of the light by the observer at time t_R . Therefore, what we observe at time t_R is in fact $\delta\theta_E$. The further away the object lies, the bigger the difference between t_E and t_R and the bigger $\delta\theta_E$ we observe. The exact turnover between these two opposite effects depends on the expansion history of the Universe as well as on the way in which light propagates in the Universe which depends on the density parameters of its different components. As seen previously, these quantities are related to each other through the Friedmann equations (Eq. 6a and Eq. 6b).

The luminosity distance Another way of measuring cosmological distances is through the luminosity distance d_L . The luminosity distance to a source is determined by comparing the known (bolometric) luminosity of the source L_s to the observed (bolometric) flux F_{obs} , which are related to each other through

$$F_{obs} = \frac{L_s}{4\pi d_L^2}. \quad (40)$$

(Objects, like Type Ia supernovae, with known luminosities are referred to as “standard candles”.)

In an expanding Universe, the expression for F_{obs} can be generalised by assuming that the source is located at the centre of a spherical shell of comoving radius $\chi(a)$. The flux observed by an observer on this spherical shell is then given by

$$F_{obs} = \frac{L(\chi)}{4\pi\chi^2(a)}, \quad (41)$$

where $L(\chi)$ now corresponds to the total luminosity passing through the comoving spherical shell. If we assume, for simplicity, that all the photons emitted by the source have the same energy, then $L(\chi)$ corresponds to the energy of one photon multiplied by the number of photons passing through the comoving shell per unit time.

Due to the expansion of the Universe, the number of photons passing through the comoving shell per unit time is smaller at the time of observation t_0 than at the time of emission t_e , by a factor $a(z_e)$. Additionally, the energy of each individual photon also decreases by a factor $a(z_e)$ between the times of emission and observation due to the Universe's expansion. Therefore, by combining these two effects, we find that the luminosity observed at a distance $\chi(a)$ from the source is a factor $a^2(z_e)$ smaller than the luminosity at the source, such that the flux observed in an expanding Universe can be rewritten as

$$F_{obs} = \frac{L_s a(z_e)^2}{4\pi\chi^2(a)}, \quad (42)$$

where L_s corresponds to the intrinsic luminosity of the source such that $L(\chi) = L_s a(z_e)^2$.

Therefore, relating Eq. 40 and Eq. 42, we find that the luminosity distance is defined theoretically in terms of the comoving distance as

$$d_L = \frac{\chi(a)}{a(z_e)}. \quad (43)$$

By substituting the definition of the comoving distance as a function of redshift (Eq. 33) and using $a = 1/(1+z)$ we therefore find that, from a theoretical point of view, the angular luminosity distance is defined as

$$d_L(z) = \frac{1+z}{H_0} \int_0^z \frac{dz'}{\sqrt{\Omega_r(1+z)^4 + \Omega_m(1+z')^3 + \Omega_k(1+z)^2 + \Omega_\Lambda}}. \quad (44)$$

Both the angular diameter distance and the luminosity distance can be determined independently from observable quantities or theoretically under the assumption of the Λ CDM model. Since at a given redshift, the observational and theoretical distance estimations must coincide, these two different definitions can be used to fit the parameters of the Λ CDM model. The late-time fit of the Hubble constant, which is based on comparing measured distances to SNe Ia sources and to their theoretically expected counterparts, is based on this principle.

2.4.3 The cosmological distance ladder

As discussed in the previous section, the luminosity distance to distant objects of known intrinsic luminosity can be determined from the measurement of their observed flux. In practice, astronomers do not measure the luminosity and the flux of objects directly but use the apparent magnitude m and the absolute magnitude \mathcal{M} instead. The apparent magnitude, which is expressed in magnitudes (mag), is a logarithmic measure of the flux received on Earth from a source. The absolute magnitude, also commonly expressed in magnitudes (mag), is a measure of the intrinsic luminosity of a source and is defined as the apparent magnitude the source would have if it were located at a standard distance of 10 pc. The luminosity distance, expressed in pc, is given in terms of m and \mathcal{M} of a source by

$$d_L = 10^{(m-\mathcal{M})/5+1}. \quad (45)$$

No single method can be used to accurately determine the absolute magnitude of different standard candles over all relevant cosmological scales. Different observation techniques have therefore been developed to be adapted to the particularities of each cosmological scale and each type of standard candle. The distances to increasingly distant objects are consequently measured using a succession of methods which altogether correspond to the “cosmological distance ladder”. These different methods are then calibrated to one another to obtain a smooth and consistent estimation of distances across all cosmological scales.

Supernovae distance measurements rely on a three-rung distance ladder. In the first rung, the distances to standardized Cepheid variable stars are measured. In the second rung, the distance measurements to Cepheids and SNe Ia are calibrated to one another using nearby galaxies containing both types of objects. In the third rung, the distances to supernovae in the Hubble flow are measured using the previously calibrated method.

Variable stars Variable stars are stars whose brightness fluctuates with a well-defined, stable period and amplitude. Amongst the different types of variable stars, Cepheids are favoured as primary distance indicators to calibrate the distance measurements of supernovae. Cepheids pulsate with a period that can range from a few days to a few months. This fluctuation is due to the periodic contraction of the surface layers of the star which causes variations in both its size and its temperature.

The brightness fluctuation period of Cepheids is tightly correlated to their absolute magnitude, as described by the Leavitt law [24], such that

$$\mathcal{M} = -\alpha - \beta \log P, \quad (46)$$

where α and β are two constants which can be calibrated using other nearby Cepheids whose distances are found using alternative methods and P is the period in days.

Therefore, the intrinsic luminosity of a Cepheid star can be determined by observing its pulsation period which in combination with the observed apparent magnitude yields the luminosity distance of the star through Eq. 45. The fact that they are very luminous objects and have a period-luminosity which is well understood makes Cepheids easy to identify and leads to extremely precise measurements of their distances ($\sim 3\%$ in distance per source) [31].

Type Ia supernovae Type Ia supernovae are a particular type of supernovae which occurs when a white dwarf found in a binary star system explodes. White dwarfs are stellar core remnants of low to intermediate-mass stars. They are primarily composed by a degenerate electron gas which is responsible for their internal pressure. When a white dwarf within a binary system starts to accrete mass from its companion star, it gradually approaches the critical Chandrasekar mass. The accreted mass causes the density and pressure within the stellar remnant to increase such that its core heats up and eventually reaches the ignition temperature for carbon fusion. The initiation of this nuclear fusion reaction causes a large portion of the matter in the white dwarf to undergo a runaway thermonuclear reaction which releases enough energy for the stellar remnant to unbind in a supernova explosion.

The nuclear reactions leading up to these supernovae explosions are ignited at a fixed critical mass closely before the white dwarf reaches the Chandrasekhar limit. For this reason, SNe Ia explosions are expected to produce, at their peak, a fairly constant luminosity, which has been verified empirically [7]. There is only a small variation in their peak luminosity which has been found to be correlated with the decay rate of the luminosity such that it can be corrected for [28]. The intrinsic luminosity, and thus the absolute magnitude, of SNe Ia can therefore be determined with high accuracy allowing them to be used as standard candles to measure distances.

Again, combining the absolute magnitude with the apparent magnitude yields the luminosity distance through Eq. 45. The magnitudes of SNe Ia can be standardized with a precision of 0.1 mag leading to distance estimations of very high precision ($\sim 5\%$ in distance per source) [8]. At its peak, the luminosity of a supernova can be as high as that of an entire galaxy allowing SNe Ia to be observed over large survey volumes which reduces the impact of local flows on our distance measurements. In addition, SNe Ia tend to occur in all types of galaxies, which is not the case for other types of supernovae, and with equal likelihood throughout the entire star forming region of the galaxy. Since their progenitors white dwarfs correspond to the final evolutionary state of a star's main sequence, SNe Ia exist in a region of the galaxy remote from where the star was originally born.

3 Estimation of the Hubble constant

Most of the cosmological parameters on which we rely to describe the geometry of the Universe are not predicted by any fundamental theory. Fitting values for these parameters requires two different observables which can be measured independently and are related to each other through the (assumed) cosmological model describing the Universe.

3.1 The observed Hubble diagram

As mentioned previously, in the case of the late-time estimation of the Hubble constant, we make use of independent measurements of the distance and the redshift z of Type Ia supernova samples. Under the assumption of the FLRW metric, these two quantities are related through the H_0 -dependent redshift-distance relationship $D(z|H_0)$ often displayed in the form of a Hubble diagram. Estimating the Hubble constant therefore comes down to fitting $D(z|H_0)$ to the observed Hubble diagram.

However, the FLRW metric strictly describes a homogeneous and isotropic Universe. In our inhomogeneous Universe, the effects of large-scale structure on the propagation of light additionally have to be taken into account when analysing observed samples. This approach therefore relies on the assumption that the FLRW model adequately describes the expansion history and dynamics of the Universe and that *on average*, light beams propagate as if the Universe is purely homogeneous, despite its inhomogeneities. This postulate is not self-evident and requires a more thorough understanding of the effect of lensing and peculiar velocities on the observed Hubble diagram.

3.1.1 The impact of peculiar motions on the Hubble diagram

When using the observed redshift-distance relationship from SNe Ia to estimate the Hubble constant, the cosmological redshift \bar{z} of the sources, which is exclusively a consequence of the Universe's expansion, should be used. In a homogeneous and isotropic Universe, the large-scale motions of galaxies (and therefore of the supernovae) purely follow the Hubble flow of the Universe's expansion, such that they lay still on a comoving grid. The observed redshift z_{obs} is then equal the cosmological redshift \bar{z} and the coming distance to a source is given by $\chi(\bar{z}) = \chi(z_{obs})$ where $\chi(z)$ is defined in Eq. 33.

In the low-redshift limit ($z \ll 1$), the comoving distance simplifies to

$$\chi(\bar{z}) = \frac{\bar{z}}{H_0}. \quad (47)$$

The redshift of the source is defined as

$$\bar{z} \equiv \frac{\lambda_{obs}}{\lambda_{em}} = 1 = \sqrt{\frac{1 + \bar{v}/c}{1 - \bar{v}/c}} - 1 \approx \frac{\bar{v}}{c}, \quad (48)$$

where λ_{obs} and λ_{em} are respectively the wavelength of the light observed and emitted by the source and \bar{v} is the receding velocity of the galaxy caused purely by the expansion of the Universe (called the Hubble flow).

Substituting this approximation for the redshift (and setting $c = 1$) we therefore recover the well-known Hubble Law which is valid at low redshift

$$\bar{v} = \chi \cdot H_0. \quad (49)$$

Therefore, in a homogeneous and isotropic expanding Universe, every observer sees all galaxies recede radially at a speed proportional to their redshift.

In reality, as described in section 2.2, the Universe is inhomogeneous and anisotropic on large scales and the scalar perturbations in the metric which couple to perturbations in the density field give rise to the large-scale structure that we observe. These density field perturbations are also associated with perturbations in the Universe's gravitational field which deflect galaxies from the pattern of motion dictated by the Hubble flow. These deviations from the pure Hubble expansion resulting from perturbations in the density field are called peculiar motions. Different forms of peculiar motions arise on different scales. On large scales, groups of galaxies (and the supernovae they host) collectively fall into larger galaxy clusters or superclusters. These groups of galaxies which conjointly move in coherent flows, tend to have correlated peculiar velocities. On smaller scales, within galaxies clusters, individual galaxies exhibit virialized motions with respect to the cluster's centre of mass. These virialized motions cause the galaxies in the same cluster to have random, uncorrelated peculiar velocities. These peculiar velocities are typically of the order of several hundreds of km/s.

In the same way that the cosmological redshift \bar{z} is related to the receding velocity of the Hubble flow \bar{v} (Eq. 48), the radial component of the peculiar velocity v_{pec} is associated with a peculiar redshift z_{pec} . Therefore, a direct consequence of peculiar motions is that the redshift observed in an inhomogeneous Universe is not equal to the cosmological redshift. Instead, as given in [12], z_{obs} , \bar{z} and z_{pec} are related through

$$(1 + z_{obs}) = (1 + \bar{z})(1 + z_{pec}). \quad (50)$$

The contribution of peculiar velocity is particularly important at low z : it can contribute to 10% of the total observed recession velocity at $z \sim 0.01$ [27]. Moreover, the effect of correlated peculiar velocities in coherent flows is also more significant at low redshifts where the physical

separation between sources, as a function of the angular separation on the sky, is smaller.

Therefore, particularly at low redshifts, the contribution of the peculiar redshift to the total observed redshift contaminates the Hubble diagram: small-scale virial motions introduce a random scatter in it and, more importantly, large-scale coherent flows lead to correlated systematic errors in certain regions of the Hubble diagram. Neglecting the correlations between supernovae peculiar motions also underestimates the uncertainty on the estimated cosmological parameters. As shown by [11], a low redshift bias of 5×10^{-4} can propagate to an error of 1 km/s/Mpc in H_0 . The biases introduced by peculiar motions in the low redshift part of the Hubble diagram can therefore not be overlooked and have to be corrected for.

3.1.2 The impact of gravitational lensing on the Hubble diagram

Gravitational lensing is the effect through which the gravitational potential resulting from the inhomogeneous density field interferes with the path on which light propagates. When a bundle of light rays emitted by a source propagates through the inhomogeneous Universe, each light ray is deflected in a slightly different way, causing the source to appear deformed and magnified. This deformation can be described by the Jacobian of the transformation from the position of the source plane β to the position of the observed source θ . The elements of this Jacobian, which is called the magnification matrix, are given by

$$\mathcal{M}_{ij} = \frac{\partial \theta_i}{\partial \beta_j}. \quad (51)$$

Instead of the magnification matrix, we often consider its inverse called the distortion matrix which relates the observed shape of the source with its real shape. The distortion matrix can be expressed in terms of the second derivative of the lensing gravitational potential $\phi(\theta)$ related to the large-scale distribution of matter, as follows

$$\mathcal{D}_{ij} = \frac{\partial \beta_i}{\partial \theta_j} = \mathcal{I}_{ij} - \frac{\partial^2 \phi}{\partial \theta_i \partial \theta_j}, \quad (52)$$

where \mathcal{I}_{ij} are the components of the 2×2 identity matrix. This 2×2 symmetric matrix can be decomposed into a symmetric part with non-zero trace and a traceless anti-symmetric part

$$\mathcal{D} = \mathcal{I} - \begin{pmatrix} \kappa & 0 \\ 0 & \kappa \end{pmatrix} - \begin{pmatrix} \gamma_1 & \gamma_2 \\ \gamma_2 & -\gamma_1 \end{pmatrix}, \quad (53)$$

such that the distortion of the shape of an object caused by lensing can be described by 3 parameters, κ , γ_1 and γ_2 . For the present analysis, we are mostly interested in the convergence κ which describes whether the source is magnified ($\kappa > 0$) or demagnified ($\kappa < 0$). The parameters γ_1 and γ_2 are related to the shear distortion of the source and describe respectively how much it is stretched or squashed in the horizontal or the vertical direction.

As a consequence of gravitational lensing, the apparent solid angle subtended by a source is not only a function of its redshift, but also depends on the matter lying on the its line-of-sight causing it to be demagnified or magnified. Since gravitational lensing preserves the surface brightness of the source, the received flux density of magnified sources (lying on over-dense lines-of-sight) is higher than the true source flux while that of demagnified sources (lying on underdense lines of sight) is lower than the true source flux. Gravitational lensing therefore compromises our distance measurements by making magnified sources appear closer than they really are and demagnified sources further away.

For this reason, the apparent distance to sources lying on a constant- z plane is effectively a varying quantity in an inhomogeneous Universe, which translates into a scatter in the observed Hubble diagram. Moreover, the scatter introduced by lensing in distance measurement is redshift-dependent. At low redshifts, where the line-of-sight to the observed source is shorter and there is less intervening matter, the dispersion in distances is mainly dominated by peculiar velocities. The effect of lensing becomes increasingly significant as we push observations to higher redshifts such that the scatter introduced by gravitational lensing in the observed Hubble diagram is redshift-dependent.

3.1.3 Reconstructing an unbiased Hubble diagram

In order to achieve an unbiased estimation of H_0 , observed samples of SNe Ia first need to be resampled in a way which ensures that the Hubble diagram constructed from them is free of any of the biases introduced by peculiar motions and gravitational lensing.

As discussed previously, peculiar motions primarily affect the low-redshift end of the Hubble diagram. Therefore, the simplest way to eliminate the bias caused by peculiar motions, without having to individually correct each redshift measurement, is to apply a low-redshift cut-off and discard all observed supernovae with redshifts below that value.

For an observed flux, the general probability distribution function (PDF) associated with lensing has a skewed, non-Gaussian shape. It is characterised by a negative mode (the received flux of most sources is slightly below the real source flux) with a long positive tail of a few sources whose received flux is significantly higher than their true source flux. However, due to the conservation of photon number, the average of this distribution coincides with that received in a FLRW homogeneous Universe [21]. This means that the average received flux of a sufficiently large sample of sources observed at constant redshift converges to the true, unlensed source flux. This property, in combination with the Central Limit Theorem, can be used to mitigate the scatter introduced by lensing in the Hubble diagram by “gaussianizing” the lensing PDF [2].

Suppose that $\{x_1, x_2, \dots, x_n\}$ is a sequence of N independent and identically distributed random samples which represent observed supernovae distances. Even if the underlying distribution of

these observations is not Gaussian, because they are affected by lensing, the Central Limit Theorem established that the probability distribution of the sample mean \bar{x}_N of these observations converges to a Normal distribution for large N . By virtue of the Central Limit Theorem, dividing large sets of observed supernovae in multiple redshift bins and subsequently computing the mean redshift and mean distance of each bin, therefore provides a way of obtaining “gaussianized” pairs of observed SNe Ia redshift and distance measurements which can be used to construct an unbiased Hubble diagram.

In addition to binning the supernova samples, it is important to use the appropriate distance indicator to construct the observed Hubble diagram [15]. Since lensing preserves the mean flux density of sources at constant redshift, only distance indicators which are linear functions of the flux density will also on average have the same value as in a homogeneous Universe. The luminosity distance d_L is related to the flux density F by $F \sim d_L^{-2}$ through the cosmological inverse square law. Therefore, $D = d_L^{-2}$ (with d_L as defined in Eq. 44) should be used as a distance indicator in the binned Hubble diagram to achieve an unbiased estimation of H_0 [2].

Specifically which low-redshift cut-off and binning parameters are used to construct the SNe Ia samples to estimate H_0 differ for each of the three biases caused by supernova blocking that we seek to study in this work. Therefore, these specifics are presented more in detail at the beginning of each of their respective sections (Section 5.1, Section 6.1 and Section 7.1).

3.2 Markov Chain Monte Carlo (MCMC) technique for parameter inference

To find the best fit parameters for the observed relationship between $D = d_L^{-2}$ and z we use a Markov chain Monte Carlo (MCMC) approach, which is a parameter inference method based on Bayesian statistics.

3.2.1 Bayes’ Theorem

Through cosmological observations, we only have access to one realisation of the Universe. We can, therefore, not rely on a frequentist interpretation of statistics in which the concept of probability is intrinsically related to the frequency of events in a number of independent realisations of a random process. Alternatively, in cosmology, we have to make use of a Bayesian approach to statistics which is useful when we only have access to one realisation of a random process which cannot be reproduced. In Bayesian statistics, the concept of probability is instead interpreted as a “degree of belief” related to our state of knowledge concerning an event.

Bayesian statistical methods rely upon Bayes’ theorem. For a given data set y and a theoretical model $M(x|\theta)$, parameterized by a set of parameters θ , describing the underlying process which generates the observed data, Bayes’ theorem provides a way to obtain the probability

distribution of the parameters of the model. According to Bayes' theorem

$$P(\theta|y, M) = \frac{P(y|\theta, M) P(\theta|M)}{P(y|M)}, \quad (54)$$

where:

- $P(\theta|M)$, the *prior probability* of the model, describes the probability of the different parameterizations of the model before the data is taken into account. In cosmology, if we assume that the Universe can be described by the Λ CDM model parameterized by some values of $\theta = [\Omega_{m,0}, H_0]$, the prior probability can be understood as the inherent likeliness of each parameter set θ . Determining the prior probability is not always straightforward. We often choose a flat prior in which we assume that before including any data, the parameters are drawn from a Uniform distribution in their respective intervals of parameter space such that all possible models have an equal prior probability.
- $P(y|M)$ is called the (*Bayesian*) *evidence* of the model. The evidence depends only on the data and the assumed model but not on the specific set of parameters considered. This term does not enter into determining the probability of the different possible parameter sets. When conducting a parameter estimation in the parameter space of a single model, the Bayesian evidence can be interpreted as a normalisation constant and is therefore often disregarded. Without loss of generality, we can then set $P(y|M) = 1$.
- $P(y|\theta, M) = L(y|\theta)$ corresponds to the *likelihood function*. This probability quantifies the compatibility of the observed data with each set of parameters. The prior probability is upgraded through the likelihood when the observed data is taken into account.
- Finally, $P(\theta|y, M)$ corresponds to the *posterior probability* of the model. The posterior probability gives the probability that a specific set of parameters accurately describes the observations for a given model. While the likelihood function is a function of the data, the posterior probability is a function of the parameters of the model.

Setting $P(y|M) = 1$, Bayes' theorem therefore simplifies to

$$P(\theta|y, M) = L(y|\theta) \cdot P(\theta|M). \quad (55)$$

Finding the parameters $\theta = [H_0, \Omega_0]$ for which the assumed cosmological model has the highest probability of describing our observations therefore relies upon Bayes' theorem. The most probable set of parameters are those for which $P(\theta|y, M)$ is maximized. If the prior is assumed to be flat, this is equivalent to maximizing the likelihood function.

3.2.2 The Likelihood function

We assume that the n observed data points y_i are independent and distributed each according to a Normal distribution of mean μ_i and standard deviation σ_i

$$y_i \sim \mathcal{N}(\mu_i, \sigma_i), \quad i = 1, \dots, n. \quad (56)$$

The likelihood function of each of the observed data points is therefore given by the probability density function of the Normal distribution

$$L(y_i|\mu_i, \sigma_i) = \mathcal{N}(y_i; \mu_i, \sigma_i) = (2\pi\sigma_i^2)^{-1/2} \cdot \exp\left\{-\frac{1}{2}\frac{(y_i - \mu_i)^2}{\sigma_i^2}\right\}. \quad (57)$$

The likelihood function of the observed dataset $L(y|\mu, \sigma)$ is given by the joint probability density of the total data set. Since the data points are assumed to be independent, their joint probability density is given by the product of their individual probabilities, such that

$$L(y) = \prod_{i=1}^n L(y_i|\mu_i, \sigma_i) = \prod_{i=1}^n (2\pi\sigma_i^2)^{-1/2} \cdot \exp\left\{-\frac{1}{2}\frac{(y_i - \mu_i)^2}{\sigma_i^2}\right\}. \quad (58)$$

In the particular case of estimating H_0 from supernovae observations, the observed data set y consists of SNe Ia distance measurements. More specifically, we use the unbiased distance observable $D = d_L^{-2}$ put forward in the previous section. The standard deviation of the Normal distribution from which each data points is assumed to be drawn (Eq. 56) corresponds to the total error associated with each observation. The mean of this distribution corresponds to the value for y_i predicted by the assumed model. In this case, the expected theoretical distance $\bar{D} = \bar{d}_L^{-2}$, which depends on the cosmological parameters $\theta = [H_0, \Omega_m]$ we want to estimate, is given by

$$\bar{D}(z|\theta) = \bar{d}_L^{-2} = \left[\frac{1+z}{H_0} \int_0^z \frac{dz'}{\sqrt{\Omega_m(1+z')^3 + (1-\Omega_m)}} \right]^{-2}. \quad (59)$$

This expression corresponds to the definition of the luminosity distance given in Eq. 44 with the additional assumptions that $\Omega_r \approx 0$ and $k = \Omega_k = 0$ which characterize the Λ CDM model.

Therefore, the likelihood function used to estimate H_0 from SNe Ia distance measurements takes the form

$$L(D|\theta) = \prod_{SN} (2\pi\sigma_D^2)^{-1/2} \exp\left\{-\frac{1}{2}\frac{(D - \bar{D})^2}{\sigma_D^2}\right\}. \quad (60)$$

The product in the likelihood function of Eq. 60 runs over the average $\langle D \rangle_{bin} = \langle d_L^{-2} \rangle_{bin}$ of each redshift bin in the supernova sample, as discussed in Section 3.1.3. The error σ_D therefore

corresponds to the error on this mean, which for a redshift bin containing N sources is given by

$$\sigma_D = \frac{\sigma_{bin}}{\sqrt{N}} = \frac{\sqrt{\sum_i^N (D_i - \langle D \rangle_{bin})^2 / (N - 1)}}{\sqrt{N}}. \quad (61)$$

In order to reduce the computational cost of evaluating this likelihood function, it is customary to work with the logarithm of the likelihood function instead, which is given by

$$\ln L(D|\theta) = -\frac{1}{2} \sum_{SN} \left[\ln(2\pi\sigma_D^2) + \frac{(D - \bar{D})^2}{\sigma_D^2} \right]. \quad (62)$$

3.2.3 Markov Chain Monte Carlo sampling

As discussed previously, the posterior probability distribution of the parameters $\theta = [H_0, \Omega_m]$ is given by the product of the likelihood function and the prior distribution (Eq. 55). By evaluating the posterior at multiple different points $\theta_i = [H_{0,i}, \Omega_{m,i}]$ in parameter space, we can estimate the posterior probability distribution and thus the most probable values for the parameters.

The most common method to sample systematically and randomly from an arbitrary posterior is by means of a Markov Chain Monte Carlo (MCMC) algorithm. The purpose of an MCMC algorithm is to construct an efficient “chain” of successive points through parameter space at which the posterior is evaluated. Monte Carlo methods enclose a large category of computational algorithms that use repeated random sampling to approximate a specific quantity. In probability theory, a Markov chain is defined as a sequence of random variables $\theta_1, \theta_2, \dots$, for which the probability of moving from a point θ_n to a subsequent point θ_{n+1} given all θ_i with $i < n + 1$ depends only on the point θ_n , such that

$$Pr(\theta_{n+1} = x | \theta_1 = x_1, \theta_2 = x_2, \dots, \theta_n = x_n) = Pr(\theta_{n+1} = x | \theta_n = x_n). \quad (63)$$

Therefore, the position of each subsequent point in a Markov chain can be computed using the information of the present position only, which is why Markov chains are sometimes called “memoryless”. Another important property of Markov chains is that the probability distribution of each new point is improved with respect to the probability distribution of the previous point such that the chain eventually converges to a stationary state where the probability distribution of the sampled points corresponds to the posterior distribution $P(\theta|y, M)$. Hence, the combination of these two processes, called a Markov Chain Monte Carlo, gives us a general method to estimate the target posterior distribution through successive random draws of θ from approximate distributions which are progressively corrected.

In parallel to the Markov chain, a criterion needs to be established to decide whether each new point θ_{n+1} is accepted or rejected depending on whether it brings the chain closer to the targeted posterior distribution. The family of Markov chain simulations which include an acceptance/rejection rule to bring the chain to converging to the posterior are called Metropolis-

Hasting algorithms.

A basic Metropolis-Hastings algorithm consists of the following steps [18]:

1. Initialization (for step $t = 0$):
 - (a) Choose an arbitrary starting point θ_0 for the chain which satisfies $P(\theta_0|y, M) > 0$. This starting point can be drawn from a starting distribution or it can be picked based on an alternative crude estimation of the best values for θ .
 - (b) Choose an arbitrary probability distribution $Q_0(\theta_1|\theta_0)$, called a proposal distribution, that suggests a point for the next step of the chain θ_1 based on the initial point of the chain θ_0 . It is customary to let $Q_0(\theta_1|\theta_0)$ be a Gaussian distribution centred at θ_0 such that points neighbouring θ_0 have a higher probability of being picked at the next step. The sequence of points therefore becomes a random walk through parameter space.
2. Iterations (for each step $t > 0$ in the chain):
 - (a) Randomly draw the next proposed point θ_p from the proposal distribution $Q_t(\theta_p|\theta_{t-1})$.
 - (b) Calculate the following ratio of probabilities:

$$\alpha = \frac{P(\theta_p|y, M)/Q_t(\theta_p|\theta_{t-1})}{P(\theta_{t-1}|y, M)/Q_t(\theta_{t-1}|\theta_p)}. \quad (64)$$

The chain can only move from the point θ_{t-1} to θ_p if both $Q_t(\theta_p|\theta_{t-1}) > 0$ and $P(\theta_{t-1}|y, M) > 0$, such that this ratio is always defined.

- (c) Decide whether to accept or reject this new proposed point θ_p . This decision is made by drawing a random number u from a Uniform distribution $U[0, 1]$. If $u \leq \alpha$, then the new point proposed is accepted such that $\theta_{t+1} = \theta_p$. Otherwise, if $u > \alpha$ the new point proposed is rejected and $\theta_{t+1} = \theta_t$, such that the chain remains at the same position.

The acceptance/rejection rule of the Metropolis-Hastings algorithm is such that if the posterior probability of the new point proposed at each step has a higher posterior probability than the previous point (such that $\alpha > 1 \geq u$) the proposed point is always accepted. However, if the new point proposed has a lower posterior probability than the previous point, there is still a chance that the proposed point will be accepted if $1 > \alpha \geq u$. The larger the decrease in posterior probability caused by the proposed point, the less likely it is that the point is accepted. Therefore, the chain mostly stays in high probability regions of the targeted posterior and only sporadically explores its low-probability regions. This explains intuitively why the algorithm successfully returns samples that are distributed according to the targeted posterior probability distribution. In addition, occasionally accepting proposed points which lower the posterior probability prevents the chain from converging to a local maximum of the parameter space and not exploring it entirely.

By following the steps outlined above, the MCMC will eventually converge to the targeted posterior distribution. However, the samples of the initial steps of the Markov chain can follow a distribution that is very different from the targeted posterior, specifically if the initial point of the chain is located in a low-probability region of parameter space. Therefore, the early steps of the chain, called the burn-in steps, are often ignored such that the dependence on the starting point is lost.

To perform the MCMC sampling under these conditions we use the `Python` package `emcee` developed by [17] to implement the Affine Invariant MCMC Ensemble Sampler developed by [19] into `Python`. We use Uniform distributions to define flat priors for both H_0 and $\Omega_{m,0}$: $H_0 \sim U[10, 100]$ and $\Omega_{m,0} \sim U[0, 1]$. The initial positions of the 100 walkers are randomly distributed around the initial guesses $\theta_0 = [70, 0.3]$. We check the convergence of the MCMC chains using `emcee` integrated tool to estimate the autocorrelation time τ after which the chain has no memory of its initial position. To ensure that the chains fully converge, the burn-in time is set to 5τ and the chains after burn-in are run for $\sim 150\tau$ steps.

4 Data

4.1 The simulated dark matter halo catalogue

The present analysis is based on a dark matter halo catalogue extracted from a relativistic N-body simulation performed with the code *gevolution* [3]. The halo catalogue is constructed from the simulated light cone using the ROCKSTAR friends-of-friends halo finder [5]. In total, it comprises about 17 million halos in the redshift range $0.001 < z < 1.27$. At low redshift ($z \leq 0.1$ corresponding to a comoving distance of 292 Mpc/h), the halos span the full sky volume. Beyond this redshift threshold, the simulated object span a conical shaped volume centred around the zenith with an opening half angle of $17^\circ 50'$. The observed redshift and observed luminosity distance of each halo are determined by integrating the geodesic equation and Sachs equation along the light ray travelling from the halo to the observer. In addition, the catalogue also contains a mass proxy for each halo in arbitrary units (corresponding to the number of N-body particles assigned to the halo).

To bypass the complications of simulating baryonic matter, we consider that there is a one-to-one correspondence between dark matter halos and galaxies. We therefore assume that each of the dark matter halos in the catalogue envelops a single galaxy in which a Type Ia supernova is observed. Additionally, we need to assign a physical radius to each of these galaxies to later be able to determine which galaxy is obstructing which supernova. This requires relating the mass distribution of dark matter halos retrieved from the simulation with the radius distribution of galaxies observed in large galaxy surveys. To do so, we use a catalogue of 50 000 galaxies observed in the Sloan Digital Sky Survey (SDSS) [1] for which the De Vaucouleurs radius has been measured. The De Vaucouleurs radius is defined to be the same as the half-light radius of the galaxy which encloses half of its total observed flux. This catalogue is constructed by selecting a $30^\circ \times 30^\circ$ field around the north galactic pole. To discard low quality data, we additionally impose that the absolute error on the radius should be smaller than 1/3 of the value of the radius. To ensure the completeness of the selected galaxy catalogue and of the distribution of galaxy radii derived from it, we only select sources in the redshift interval $z < 0.4$ and assume the radius distribution to be independent of redshift.

Abundance matching is the simplest approach to matching the observed distribution galaxy radii to the simulated distribution of dark matter halo masses. It relies, firstly, on the assumption that each dark matter halo contains a single galaxy such that the total number of galaxies and dark matter halos per unit volume are equal. Therefore, we have that

$$\int_0^\infty n_R(r) dr = \int_0^\infty n_M(m) dm, \quad (65)$$

where $n_R(r)$ is the radius number density of galaxies and $n_M(m)$ is the mass number density of halos. Secondly, we assume that there is a monotonic relationship between the mass of the host halo and the radius of the galaxy it contains.

The simulated catalogue and the observed catalogue both have some intrinsic lower threshold which are not related to each other. However, we expect that the halos with the largest masses and the galaxies with the largest radii are included in both catalogues. Therefore, the galaxies with the largest radii can be associated with the halos with the largest masses by imposing the following equality on both cumulative number densities

$$\int_{r(m)}^{\infty} n_R(r') dr' = \int_m^{\infty} n_M(m') dm'. \quad (66)$$

The dependence of the galaxy radius on the host halo mass $r(m)$ is given implicitly by this relation which therefore can be used to assign a radius to the galaxy contained by each simulated dark matter halo in the catalogue.

4.2 Statistics of galaxy/supernova blocking

The determination of which supernovae in the catalogue are obstructed by a foreground galaxy is based on two straightforward conditions. Firstly, the galaxy has to lie in the foreground of the supernova, which, in terms of their comoving distances d_C , translates to

$$d_C^{galaxy} - d_C^{SN} < 0. \quad (67)$$

We use the comoving distance which corresponds to the distance between two fundamental observers (both moving with the Hubble flow) obtained by integrating the infinitesimal δd_C of nearby fundamental observers along the line-of-sight from $z = 0$ to the observed object. The comoving distance between two objects remains constant through time, despite the expansion of the Universe, such that it is appropriate for measuring separations that are imprinted in the Hubble flow. Secondly, a supernova is obstructed by a galaxy lying in its foreground if the angular separation θ between the supernova and the galaxy is smaller than the angular radius of the galaxy α_r . Therefore, the second condition to find the blocking-galaxy / blocked-supernova pairs in the catalogue is

$$\alpha_r - \theta > 0. \quad (68)$$

In case that multiple galaxies fulfil these two conditions for the same supernova, we consider that it is blocked by the galaxy for which θ is minimal. To get a better feel for how significant this obstruction could be in large SNe Ia samples, we determine which sources in the catalogue are obstructed twice, using two different definitions for α_r . In the first case, we take a more conservative approach consider that the radius of a galaxy corresponds effectively to its half-light radius ($\alpha_r = r_{HL}$) while in the second case we consider that $\alpha_r = 2r_{HL}$ as an upper

boundary. These two definitions of the radius of a galaxy can both be appropriate depending on the “blocking scenario” under consideration. In case we consider total blocking of the supernova by the foreground galaxy, restricting the radius to $\alpha_r = r_{HL}$ is more appropriate. Taking into account the Sérsic model which describes the brightness profile of galaxies, it indeed seems unlikely that such a total blocking would take place outside the effective radius of a galaxy. However, confusing the obstructing galaxy with the host-galaxy can still happen if the supernova is visible through the outskirts of the galactic disk. Therefore, in this case, it is relevant to consider obstruction until $\alpha_r = 2r_{HL}$.

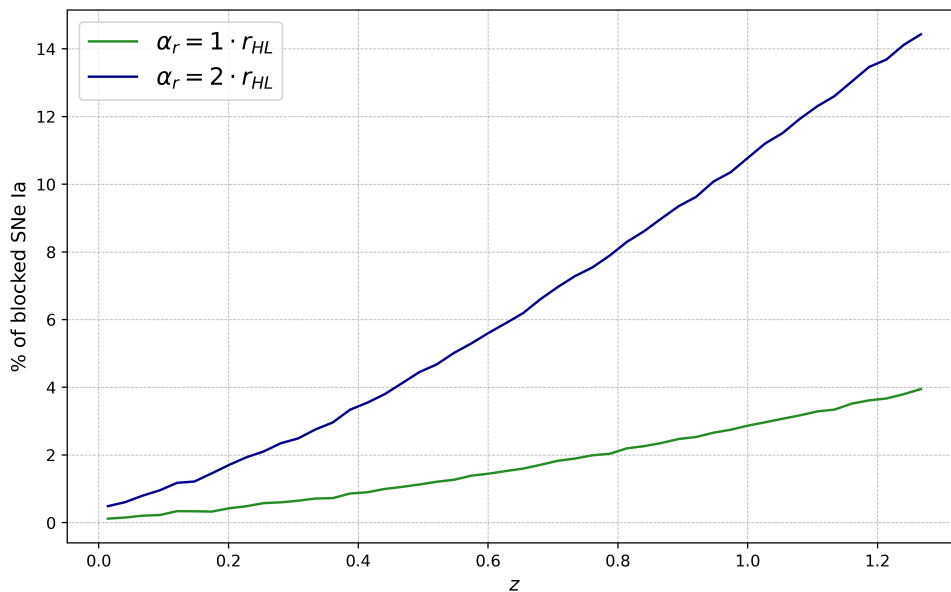


Figure 4: Percentage of obstructed supernovae in the simulated catalogue as a function of redshift, for two different definitions of the galactic radius. (Note that all the supernovae which are blocked within 1 half-light radius are also included in those blocked within 2 half-light radius.)

Fig. 4 summarizes the fraction of supernovae lying behind a galaxy, in the simulated catalogue, as a function of redshift for both definitions of α_r . When using $\alpha_r = 1 \cdot r_{HL}$ we find that 2.4% of supernovae in the whole catalogue and 3.4 % of supernovae above $z = 1$ are obstructed by a foreground galaxy. When using $\alpha_r = 2 \cdot r_{HL}$ we find that 9% of supernovae in the whole catalogue and 12.7 % of supernovae above $z = 1$ are obstructed by a foreground galaxy. Additionally, it is worth noting that a lower mass threshold is imposed to identify the dark matter halos in the simulated light cone. This causes the low mass halos to be neglected which leads to underestimating the density of small galaxies in our simulated catalogue. Therefore, the estimates of Fig. 4 are conservative and it is likely that the fraction of obstructed supernovae is somewhat higher in our observed SNe Ia samples.

For the supernovae lying behind a galaxy we then look at the distribution of the ratio d_C^{galaxy} / d_C^{SN}

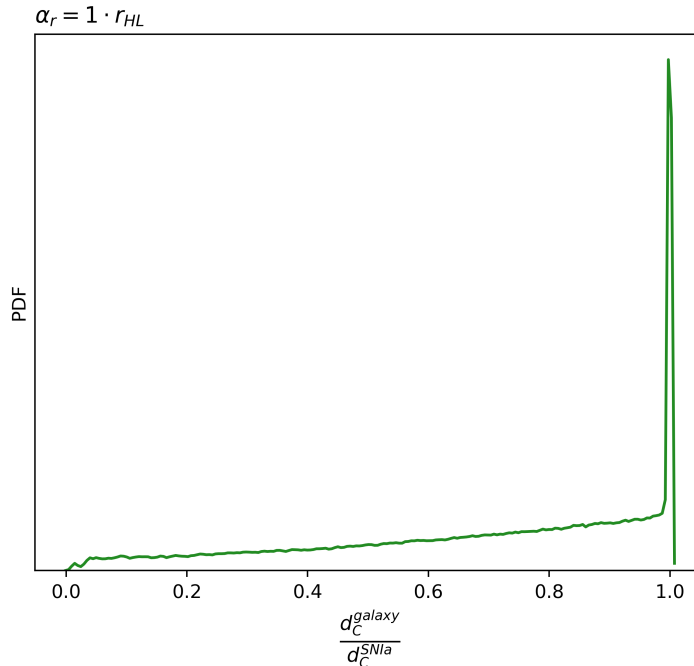


Figure 5: Distribution of the ratio d_C^{galaxy}/d_C^{SNIa} for the foreground galaxy/blocked supernova pairs found in the simulated catalogue.

which is shown in Fig. 5. This quantity indicates how close the galaxy lies to the supernova it is obstructing. The peak of this distribution lies very close to $d_C^{galaxy}/d_C^{SN} = 1$, implying that most supernovae are obstructed by a neighbouring galaxy, located in the same cluster as their host-galaxy. However, the tail of the distribution where d_C^{galaxy}/d_C^{SN} is small should not be neglected. These supernovae which are obstructed by a distant foreground galaxy are the ones which are likely to introduce a larger bias in the observed Hubble diagram. In these cases, the large separation between the supernova and the foreground galaxy makes it more likely for the light emitted by the supernova to be overpowered by that of the galaxy lying closer to us and therefore to be no longer visible to us. Otherwise, erroneously assigning the redshift of the distant foreground galaxy to the supernova, will lead to misplacing it on the Hubble diagram more significantly than if the host is confused with a galaxy within the same cluster.

Lastly, we inspect to what extent the supernovae in this obstructed sample are affected by gravitational lensing. In order to determine this, we look at the distribution of their convergence κ and compare it to that of the visible supernovae as represented in Fig. 6. As mentioned in Section 3.1, κ describes whether a source is magnified ($\kappa > 0$) or demagnified ($\kappa < 0$) due to gravitational lensing. It is defined as follows in terms of the angular diameter distance to the source in a FLRW Universe \bar{d}_A and the measured angular diameter distance to the source d_A

$$\kappa \equiv 1 - \frac{d_A}{\bar{d}_A}. \quad (69)$$

We find that the average convergence of blocked supernovae above $z = 1$ is $\langle \kappa_{obstructed} \rangle = 0.005$

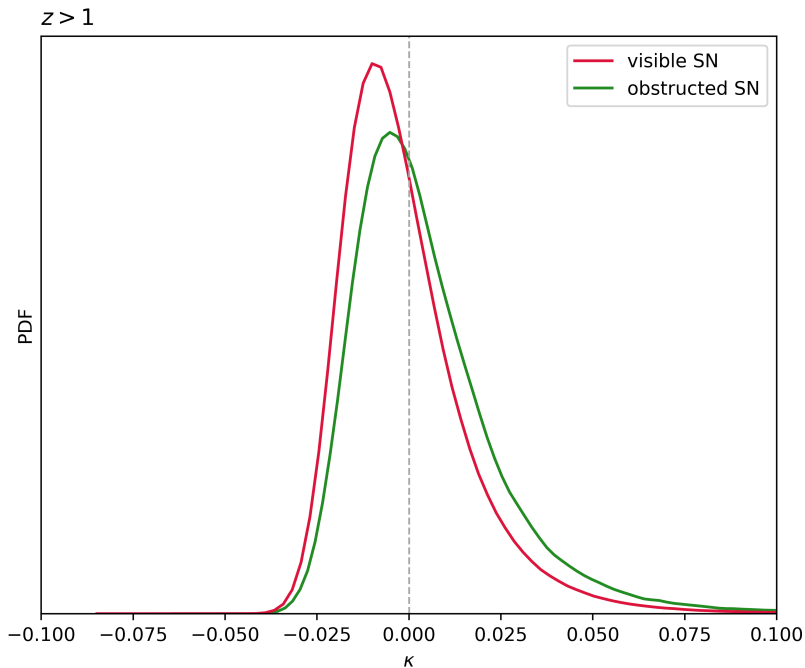


Figure 6: Distribution of the convergence parameter κ for the blocked and the visible sources above redshift $z = 1$.

while that of visible supernovae is $\langle \kappa_{visible} \rangle = -0.001$. In addition, as shown in Fig. 6, the distribution of κ is more skewed towards $\kappa > 0$ for obstructed sources than for visible sources, meaning that, on average, blocked the supernovae are more magnified than the visible ones. The reason for this is that supernovae obstructed by a foreground galaxy lie on over-dense lines-of-sight, which increases their magnification.

5 The impact of total supernova blocking on the estimation of H_0

This section is dedicated to determining the impact of the selection bias caused by the “total blocking” of certain supernovae on the estimation of H_0 . As discussed in the previous section, certain supernovae in the simulated catalogue are obstructed by a foreground galaxy. If the relative distance between both objects is large, the foreground galaxy is very bright or the supernova is aligned with the centre of the foreground galaxy, it can happen that the light emitted by the background SNe Ia is not visible to us through the intervening galaxy. In this section, we consider that all supernovae lying behind the 1 half-light radius of a foreground galaxy are no longer visible to us. As shown in Fig. 4, this corresponds to $\sim 1\%$ of the SNe Ia at $z = 0.5$ and $\sim 3\%$ of the SNe Ia at $z = 1$ in our simulated catalogue. We want to estimate the impact of the selection bias caused by these supernovae missing from our observations on the value inferred for H_0 .

5.1 Selecting an unbiased supernova sample

For the purpose of this part we use the supernovae of the simulated catalogue in the redshift range $z > 0.5$. Following the discussion of Section 3.1.3, this low-redshift cut-off is introduced as a way of mitigating the bias caused by peculiar motions on the Hubble diagram. This specific cut-off is chosen by running a trial MCMC using the full redshift range of the catalogue and identifying the redshift threshold below which the residuals no longer scatter randomly around 0.

To estimate H_0 , a random sample of 300 000 sources in this redshift range is selected from the simulated catalogue. These sources are binned into 1000 bins of equal redshift range (with $\Delta z_{\text{bin}} \simeq 8 \cdot 10^{-4}$). For each of these bins, we then compute the average redshift $\langle z \rangle_{\text{bin}}$ and the average distance $\langle D \rangle_{\text{bin}} = \langle 1/d_L^2 \rangle_{\text{bin}}$ as well as the error on $\langle D \rangle_{\text{bin}}$ according to Eq. 61. The bins which contain less than 100 sources are discarded, as they are not large enough for the Central Limit Theorem to properly “gaussianize” their mean. For this simulated catalogue, these correspond at most to a few out of the 1000 bins, depending on the specific randomly selected sources, such that this has no incidence on the subsequent estimation of H_0 .

Note that we have opted to bin the sources using bins of constant redshift range Δz_{bin} rather than bins with a constant number of sources. This approach ensures that the resulting points ($\langle z \rangle_{\text{bin}}, \langle D \rangle_{\text{bin}}$) uniformly sample the Hubble diagram across the redshift range considered. However, this decision comes at the cost of losing the information of the redshift distribution of the sample. We made the choice of prioritizing uniformly sampled points as this is more important when it comes to accurately fitting the Hubble diagram. This ensures that the extremities of the Hubble diagram, where sources are scarcer, are well sampled. This is particularly important because the fit of the Hubble diagram is very sensitive to these extreme points. This type of

binning therefore prevents any deviation in the inferred H_0 caused by the binning of the sources.

This procedure, as discussed in Section 3.1.3, produces a sample of points $(\langle z \rangle_{\text{bin}}, \langle D \rangle_{\text{bin}})$ which form a Hubble diagram exempt from the biases induced by peculiar motions and gravitational lensing. The Hubble constant can be estimated from these points following the method outlined in section 3.2.

5.2 Results

To determine the impact of the selection bias caused by blocked supernovae, we estimate H_0 using four different samples. The first two samples are different random samples selected from the simulated catalogue without regard for blocking. These samples contain both blocked and visible supernovae and act as our “control” samples. The third sample represents the case where we consider that all supernovae lying behind the 1 half-light radius of a foreground galaxy are not visible. This sample contains only sources which are visible according to this criterion. Lastly, the fourth sample represents the case where we assume that all supernovae lying behind the 2 half-light radius of a foreground galaxy are blocked. This last sample only contains sources which are visible according to this definition. The third sample is the most likely to realistically represent the blocked SNe Ia in our real observed samples while the fourth sample is the most extreme case which is probably not very realistic but should be understood as an upper boundary for supernova blocking.

Each of these samples is binned into 1000 points $(\langle z \rangle_{\text{bin}}, \langle D \rangle_{\text{bin}})$, as described previously, to estimate H_0 . The four H_0 distributions which result from these SNe Ia samples are shown in the corner plot in Fig. 7. The central parameter values of these distributions and their corresponding 68% confidence intervals are summarized in Table. 1.

The parameters estimated from the two control samples provide a valuable consistency check for the MCMC parameter estimation. The scatter of the central parameter values obtained from these two samples, which reflects the use of different sources from the catalogue, is consistent with their error ellipses (i.e. it is neither much larger nor much smaller). As expected for a robust MCMC estimation, the difference between the parameters found with these two samples is statistically negligible.

The two samples which account for supernova blocking lead to higher central values for H_0 and lower central values of Ω_m than the two control samples. The value for H_0 inferred from the third sample ($\alpha_r = 1 \cdot r_{HL}$) deviates from that obtained from the first control sample by $\sim 0.03\%$. Alternatively, these two measurements differ at a level of 1.6σ . The fourth sample ($\alpha_r = 2 \cdot r_{HL}$) yields a central value for H_0 which differs from that of the first control sample by $\sim 0.09\%$, which translates to a difference of 5σ . This higher discrepancy is to be expected since this sample represents the extreme blocking case.

The fact that the inferred value for H_0 is higher when using only visible supernovae than when using both visible and blocked supernovae implies that our estimations based on observed SNe Ia samples tend to overestimate the value of H_0 due to the blocking of supernovae by foreground galaxies.

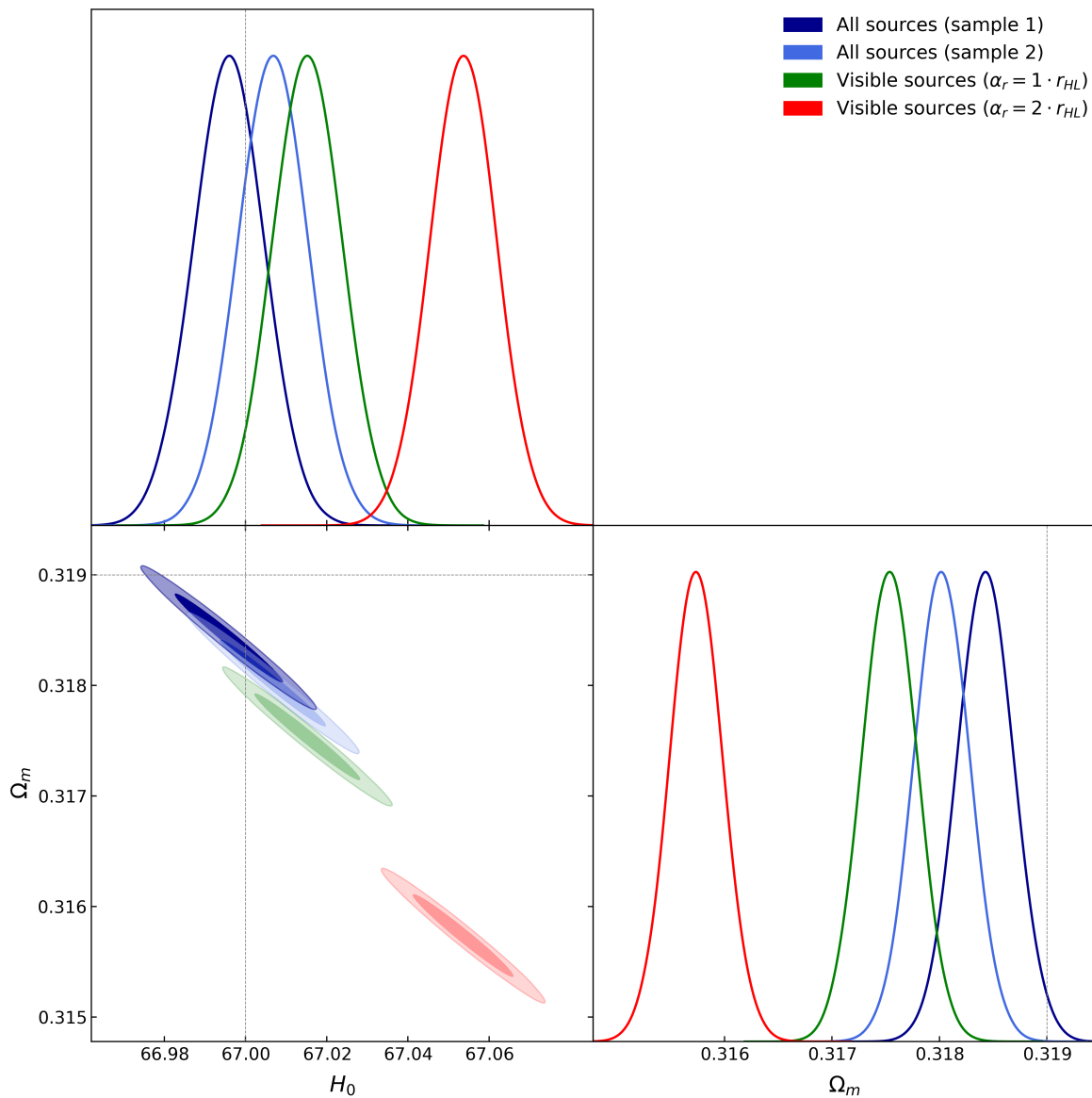


Figure 7: Corner plot of the posterior distribution of H_0 and Ω_m for 4 different SNe Ia samples. The two blue ellipses are obtained from the “control” samples without regard for blocking. The green ellipse represents the results from the sample which contains only SNe Ia that are visible when using $\alpha_r = 1 \cdot r_{HL}$. The red ellipse represents the results obtained from the sample which contains only SNe Ia that are visible when using $\alpha_r = 2 \cdot r_{HL}$. The grey lines represent the true parameter values used in the simulation.

	H_0 [km/s/Mpc]	Ω_m
all sources	66.9959 ± 0.0088	0.31843 ± 0.00026
visible sources ($\alpha_r = 1 \cdot r_{HL}$)	67.0152 ± 0.0085	0.31753 ± 0.00026
visible sources ($\alpha_r = 2 \cdot r_{HL}$)	67.0536 ± 0.0082	0.31574 ± 0.00025
true values (simulation)	67	0.319

Table 1: Summary of the central parameter values estimated from the simulated SNe Ia samples used to assess the selection bias induced by blocked supernovae.

5.3 Discussion

The increment in H_0 that we find as a consequence of SNe Ia blocking can be understood by considering the position that these blocked supernovae occupy on the fitted Hubble diagram. Fig. 8 represents the observed Hubble diagram constructed from two of the supernovae samples introduced previously: on one hand, the first sample of 300 000 sources which contains both blocked and visible supernovae and on the other hand the fourth random subsample which contains only supernovae that do not lie behind the $\alpha_r = 2 \cdot r_{HL}$ radius of a foreground galaxy. By comparing the two Hubble diagrams resulting from these different samples it becomes apparent that the blocked supernova cluster below $\bar{d}_L(z)$ mostly at high redshift. This can be explained, as mentioned in Section 4.2, by the fact that supernovae which are obstructed by a foreground galaxy typically lie on over-dense lines-of-sight such that, on average, they are more magnified than their visible counterparts. The distances to these obstructed supernovae therefore tend to be systematically underestimated, such that $d_L^{obs} < \bar{d}_L$ which is why they lie below the $\bar{d}_L(z)$ curve on the observed Hubble diagram. Additionally, the fraction of obstructed supernovae increases with increasing redshift as the number of intervening galaxies grows (see Fig. 4). As a result of these two effects combined, obstructed supernovae cluster on the high-redshift end of the Hubble diagram below the $\bar{d}_L(z)$.

The fact that the blocked supernovae are not scattered randomly across the Hubble diagram leads to a selection bias in the estimation of H_0 . Understanding more specifically how the absence of these blocked supernovae translates to the inferred values for H_0 and Ω_m is not straightforward due to the complex nature of the function being fitted (Eq. 44) which relates these two parameters. However, we verify empirically that this selection bias results in an over-estimation of the Hubble constant. The increase in H_0 goes hand in hand with a decrease in Ω_m when the blocked supernovae are excluded from the fitted Hubble diagram. In addition to being related through Eq. 44, the correlation between these two parameters can be understood in the context of the Universe’s expansion dynamics. Indeed, the expansion of the Universe is slowed down by the attractive gravitational pull of matter which counteracts the repulsive push of dark energy. Consequently, a lower matter density leads to a faster expansion of the Universe.

We notice that the 2σ ellipses of the posterior distributions found from the two samples which

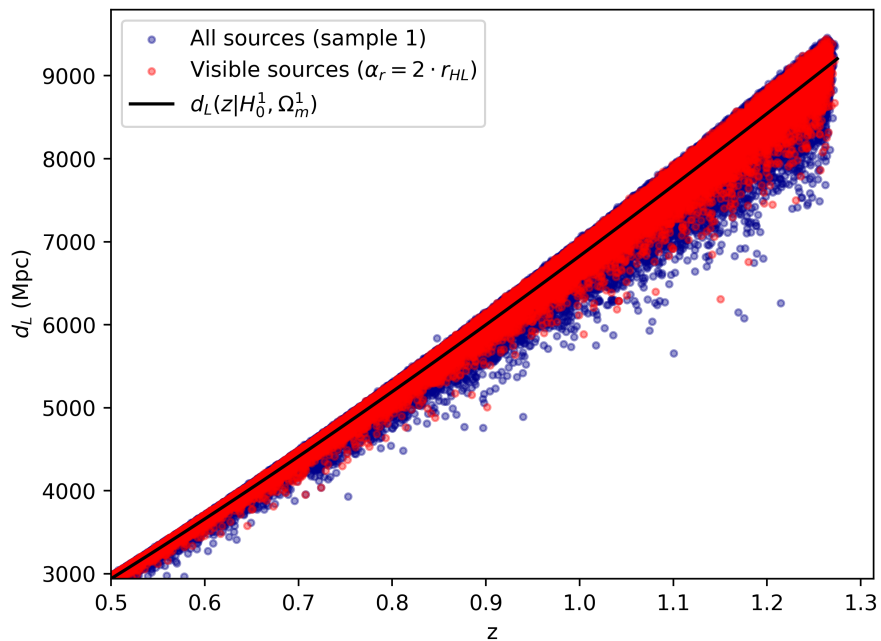


Figure 8: Hubble diagram constructed from the two different subsamples of 300 000 SNe Ia from the simulated catalogue. The $\bar{d}_L(z)$ curve is computed with the parameters used in the simulation ($H_0 = 67\text{km/s/Mpc}$ and $\Omega_m = 0.319$). (Note that the sources used to construct these Hubble diagrams have not been binned such that they are still subject to the bias introduced by gravitational lensing which is why the scatter around the $\bar{d}_L(z)$ curve is not Gaussian.)

contain both visible and blocked sources do not encompass the true parameter values of the simulation. This indicates that despite the measures taken, the binned and average Hubble diagrams constructed still retain a slight bias. An unbiased estimation of H_0 was achieved by [2] using a similar binning approach for constructing the Hubble diagram for the MCMC. However, their analysis included sources with redshifts up to $z = 3$ and the simulated sample was divided into equally sized bins containing 1000 adjacent supernovae. Therefore, it seems that the parameter values estimated from the first two control samples could be drawn nearer to the true parameters used in the simulation by increasing the number of sources within each bin to enhance the “gaussianizing” effect of the Central Limit Theorem. In addition, including more sources at higher redshift would reduce the effect of peculiar motions beyond the low-redshift cut-off, further suppressing the remaining bias. In any case, it would be interesting to look more thoroughly at how this binning procedure can be optimized to achieve an unbiased H_0 estimation using the smallest SNe Ia sample possible.

Additionally, there is a small caveat concerning the procedure described in Section 5.1 to suppress the bias introduced by peculiar velocities on the Hubble diagram which should also be mentioned. As the fraction of blocked supernovae increases with redshift, the low-redshift cut-off that was introduced might slightly amplify the effect of supernovae blocking on the H_0 estimation as we are estimating H_0 from the part of the Hubble diagram most affected by blocking. However, we still believe it is preferable to introduce this cut-off to ensure an unbiased estimation of H_0 , even if it results in a slight amplification of the blocking effect.

Moreover, the lower mass threshold imposed to construct the halo catalogue from the simulation leads to underestimating the density of small galaxies when performing the abundance matching. Consequently, we have most likely also underestimated the fraction of blocked supernovae. In any case, it is reasonable to assume that the effect of supernova blocking on the inferred value of H_0 presented here is still conservative and that this bias is likely to be more prominent when using observed supernova samples.

The results presented in the previous section imply that the selection bias caused by supernovae blocking aggravates the Hubble tension. The Hubble tension could therefore be somewhat alleviated by taking this bias into account. However, this statement should be approached with a critical mindset in light of how narrow the confidence intervals of our H_0 estimates are in comparison to the accuracy of H_0 measurements based on observed datasets. Supernova distance measurements are, to this day, dominated by statistical errors. The greatest improvement of the latest SH0ES measurements was to increase the size of the supernova sample to reach a sub-percent error on each of the error components of the H_0 estimation which combine to a total error of 1.4% [31]. The 0.03% to 0.09% discrepancy in H_0 found to be caused by blocked supernovae is significantly smaller than each of the components of the error in the SH0ES measurement. Therefore, the impact of this selection bias is not relevant yet given the precision of current H_0 estimations. However, with the imminent launch of upcoming surveys

such as the Large Synoptic Survey Telescope (LSST), we expect a substantial increase in the size of supernovae samples. This will likely shift the dominant source of error in SNe Ia distance measurements from statistical errors to systematic errors emphasizing the need for more robust consideration of systematic biases. The significance of smaller systematic errors, such as the selection bias presented here, will therefore gain importance and require more attention in the upcoming years.

6 The impact of supernova/host-galaxy mismatching on the estimation of H_0

The fact that certain supernovae lie behind a foreground galaxy does not necessarily imply that they are all missing from our observed samples. At their peak, supernovae can reach luminosities comparable to those of an entire galaxy, such that it is likely that some of the obstructed SNe Ia can still be observed through their foreground galaxy. In this section, we consider that all the supernovae from the simulated catalogue which lie behind the $\alpha_r = 2 \cdot r_{HL}$ radius of a foreground galaxy are visible to us.

The accuracy of H_0 measurements from SNe Ia observations heavily depends on our ability to accurately measure their redshifts. The preferred approach is to measure them indirectly by using the spectroscopic redshifts of their host-galaxy, which have sharper spectral lines and offer a higher accuracy. An important task is therefore to correctly associate each supernova with its corresponding host-galaxy [9]. When spectroscopic information is unavailable for the supernova, this matching process involves examining all galaxies within a radius of $\sim 30''$ around each supernova and selecting the galaxy with the minimum normalized angular separation from the supernova, considering the elliptical radius of the galaxy in the supernova's direction [20]. However, this method is susceptible to mistakes when it comes to obstructed supernovae that have very small angular separations from their foreground galaxies. In such cases, there is a risk of incorrectly associating the supernova with the obstructing galaxy rather than with its true host-galaxy and therefore assigning an incorrect redshift to the supernova. In this section we assess the impact of this host misidentification on the estimation of H_0 .

6.1 Selecting an unbiased supernova sample

Like in the previous section, we introduce a low-redshift cut-off at $z = 0.5$ to alleviate the bias caused by peculiar motions on the Hubble diagram. The binning procedure described in section 5.1 is also reproduced to correct for the effect of the non-Gaussian lensing PDF on the Hubble diagram. We select a random sample of 300 000 sources from the simulated catalogue to estimate H_0 . These sources are then divided into 1000 bins, each covering an equal redshift range ($\Delta z_{\text{bin}} \simeq 8 \cdot 10^{-4}$). Within each bin, we calculate the average redshift $\langle z \rangle_{\text{bin}}$, the average distance $\langle D \rangle_{\text{bin}} = \langle 1/d_L^2 \rangle_{\text{bin}}$, and the corresponding error using Eq. 61. Bins with fewer than 100 sources are excluded from the analysis to ensure the Central Limit Theorem can effectively “gaussianize” their mean.

As mentioned earlier, this method generates a set of points $(\langle z \rangle_{\text{bin}}, \langle D \rangle_{\text{bin}})$ which constitute an unbiased Hubble diagram, free from the biases caused by peculiar motions and gravitational lensing. The Hubble constant can be estimated from these points using the approach described in section 3.2.

6.2 Results

To assess the impact of incorrectly matching obstructed supernovae to their foreground galaxy we select one random sample from the simulated catalogue and we estimate H_0 from this sample assuming different mismatching scenarios. This sample is binned into 1000 points $(\langle z \rangle_{\text{bin}}, \langle D \rangle_{\text{bin}})$, as described previously, to estimate H_0 .

In the first scenario all supernovae are correctly matched to their true host-galaxy. Therefore, all the SNe Ia in this scenario are rightly assigned the redshift of their host-galaxy. In the second scenario, the unobstructed supernovae are also correctly matched to their true host-galaxy. However, we now account for the possibility of obstructed SNe Ia being inaccurately assigned to their foreground galaxy. The probability of mismatch is assumed to be inversely proportional to the angular separation θ between the supernova and the foreground galaxy. Specifically, when $\theta = 0$, the probability of a mismatch is $P_{MM} = 1$. This probability decreases linearly as θ increases until it reaches $P_{MM} = 0$ at $\theta = 2 \cdot r_{HL}$. Supernovae that are mismatched according to this probability law are associated with the redshift of their foreground galaxy rather than their host-galaxy. In the third scenario, we once again match the unobstructed SNe Ia to their correct host-galaxy. However, in this case, we assume that all obstructed supernovae are mistakenly matched to their foreground galaxy. As a result, all obstructed SNe Ia in this sample are assigned the redshift of their foreground galaxy.

The first scenario describes the case in which the matching between the supernovae and their host-galaxies is done 100% correctly. This case therefore serves as our “control” case against which we compare the results from the two other scenarios. The second scenario is the one which most realistically represents the extent of mismatching errors that occur in the supernova/host-galaxy matching algorithms used to analyse our observed samples. The third scenario represents the extreme case where the matching between obstructed supernovae and their host-galaxies is done 100% incorrectly. It is highly improbable for the currently used algorithms to perform this poorly, so this case serves mainly as an upper limit for the error induced by mismatching on the estimation of H_0 .

The H_0 estimations resulting from these three scenarios are shown in Fig. 9. The central parameter values and their corresponding 68% confidence intervals are summarized in Table 2. By comparing these three estimates it becomes apparent that mismatching the obstructed SNe Ia to their foreground galaxies results in underestimating H_0 and overestimating Ω_m . Assuming that the mismatch probability decreases linearly with increasing angular separation θ , leads to an estimation of H_0 which is $\sim 1.95\%$ lower than that obtained from the control case. In the extreme scenario where all obstructed supernovae are incorrectly matched, H_0 is underestimated by $\sim 6.43\%$ with respect to the control case.

	H_0 [km/s/Mpc]	Ω_m
0% mismatched hosts	66.9794 ± 0.0091	0.31888 ± 0.00028
mismatched hosts $\propto \theta$	65.673 ± 0.033	0.35042 ± 0.00091
100% mismatched hosts	62.677 ± 0.054	0.4318 ± 0.0017
true values (simulation)	67	0.319

Table 2: Summary of the central parameter values for H_0 and Ω_m estimated by assuming three different mismatching scenarios.

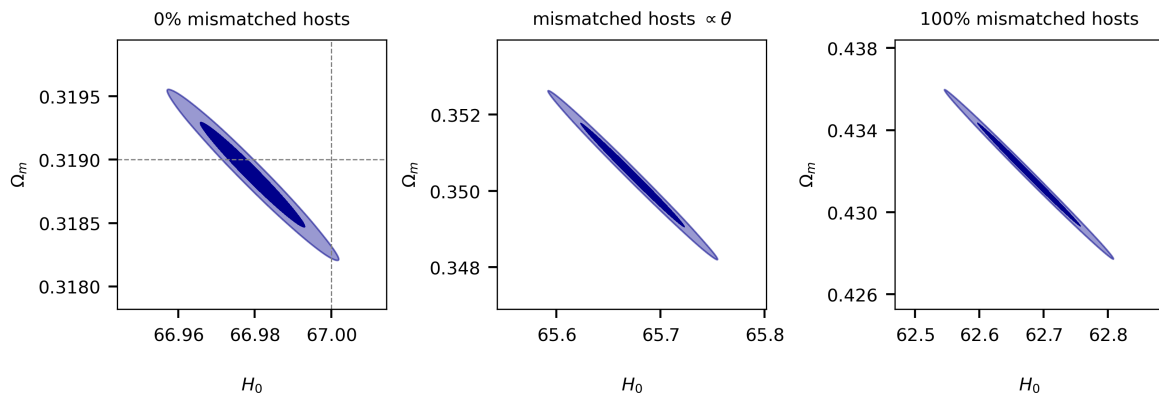


Figure 9: Constraints on H_0 and Ω_m for 3 different scenarios of host-galaxy mismatching. The left panel represents the results obtained from the control case. The grey dotted line represents the true parameter values used in the simulation. The central panel corresponds to the results obtained by assuming that the probability of mismatch is proportional to the angular separation θ between the supernova and the foreground galaxy. The results on the right panel are obtained by assuming that 100% of the obstructed SNe Ia are mismatched to their foreground galaxy.

6.3 Discussion

6.3.1 Impact of supernova/host-galaxy mismatching on the Hubble diagram

The shift in H_0 resulting from supernova/host-galaxy mismatching that we find is larger than the total error of 1.4% on the latest measurement by the SH0ES team [31]. It is therefore already relevant for our current estimations and is bound to acquire an even greater significance with the expected accuracy increase of our measurements in the upcoming years.

The decrease in the estimated value of H_0 resulting from the host-galaxy misidentification for obstructed supernovae can be understood by analysing its impact on the Hubble diagram. In Fig. 10 we plot the Hubble diagram resulting from the sources selected randomly from the simulated catalogue, assuming that the probability of mismatch decreases as the angular separation between the supernova and the foreground galaxy increases. The obstructed SNe Ia for which the host-galaxy has been misidentified are scattered across the upper-left region of the plot.

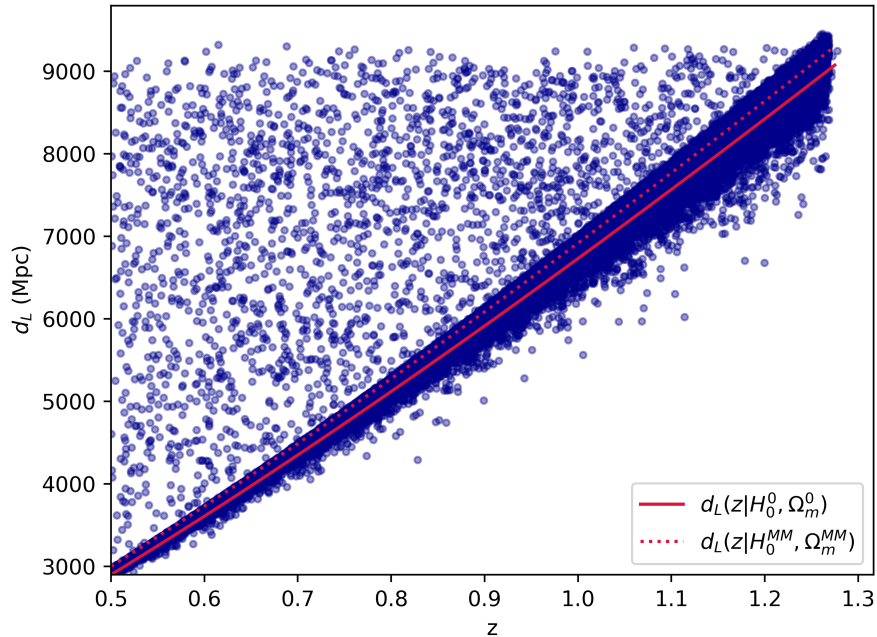


Figure 10: Hubble diagram constructed from the sample in which we assume that the probability of mismatching the obstructed supernovae to their foreground galaxy is inversely proportional to the angular separation between both sources. The full $d_L(z)$ curve is computed with the parameters fitted from the sample where all SNe Ia are correctly matched to their host-galaxy while the dotted $d_L(z)$ curve is computed with the parameters fitted from the sample used to construct the Hubble diagram (see Table 2).

Since the measured distance to these obstructed supernovae is not affected by the host misidentification, mismatched supernovae are shifted horizontally to lower z along a line of constant d_L on the Hubble diagram. These sources therefore introduce a significant bias in the Hubble diagram towards higher values for d_L at fixed z , particularly at low redshifts. The dotted line in this figure represents the $d_L(z)$ curve computed with the parameters fitted from this sample, while the full $d_L(z)$ curve is computed using the parameters fitted from the scenario in which all supernovae are correctly matched to their true host-galaxy. By comparison, we see that the mismatched supernovae “pull” d_L upwards at fixed z . We consequently find that the fit of this upwards shifted $d_L(z)$ curve results in a lower value for H_0 and a higher value for Ω_m when the host-galaxies of obstructed supernovae are misidentified.

6.3.2 Residuals of the MCMC fit

To assess the quality of the Hubble diagram fit performed by the MCMC from each case, we examine the distribution of the residuals in Fig. 11 and Fig. 12. As expected, the residuals for all three MCMC fits exhibit a Gaussian-like distribution centred around $\mu = 0$ and no particular pattern with respect to redshift. This suggests that the non-Gaussian biases introduced by lensing and peculiar velocities in the Hubble diagram have effectively been mitigated by the

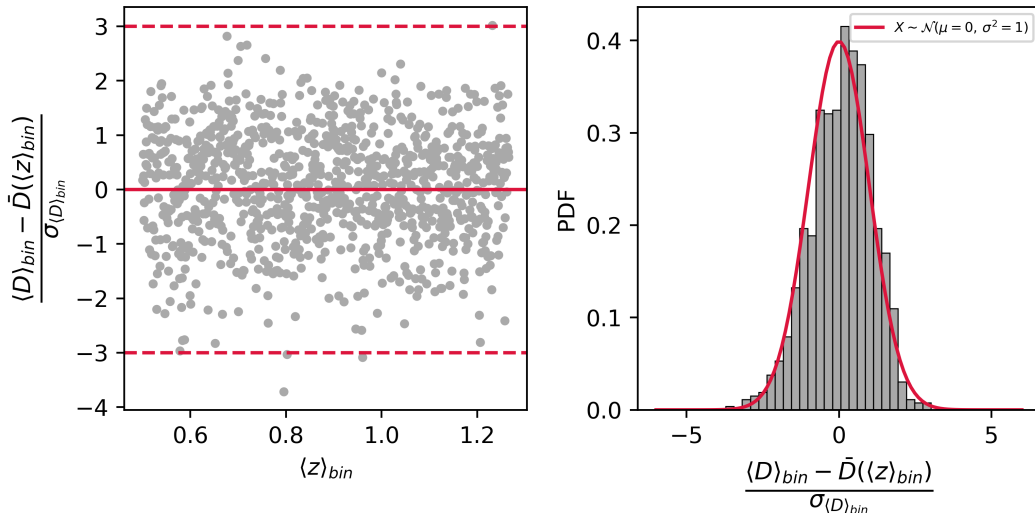


Figure 11: Residuals of the MCMC fit performed with the control sample in which the matching between the supernovas and their host-galaxies is done 100% correctly.

procedure outlined in Section 3.1.3 and Section 6.1. Moreover, the agreement of the residual distributions with a Gaussian shape substantiates the assumption of a Gaussian likelihood function for the resulting set of points $(\langle z \rangle_{\text{bin}}, \langle D \rangle_{\text{bin}})$. However, the residuals of the control case, which does not contain any mismatched supernovae, still exhibit a slight deviation from a Gaussian distribution centred at $\mu = 0$. This indicates that the binned Hubble diagram constructed for the MCMC analysis retains a small leftover bias. Consequently, the 2σ ellipse of the posterior distributions derived from this control sample does not encompass the true parameter values used for the simulation. As mentioned in Section 5.3, the small bias which persists in our control sample could probably be eliminated by using larger bins to strengthen the “gaussianizing” effect of the Central Limit Theorem. Furthermore, incorporating more sources at higher redshifts would mitigate the impact of peculiar motions beyond the lower redshift cut-off, thereby further reducing the remaining bias.

In addition, we notice distinct gaps in the residual scatter plot of the third scenario (bottom panel of Fig. 12), which appear below $(\langle D \rangle_{\text{bin}} - \bar{D}(\langle z \rangle_{\text{bin}}))/\sigma_{\langle D \rangle_{\text{bin}}} = 0$ around $z = 1$, and above $(\langle D \rangle_{\text{bin}} - \bar{D}(\langle z \rangle_{\text{bin}}))/\sigma_{\langle D \rangle_{\text{bin}}} = 0$ around $z = 0.6$ and $z = 1.2$. Therefore, the gap around $z = 0.6$ in the residual scatter plot corresponds to obstructed SNe Ia that fall below the $z = 0.5$ cut-off after the host-galaxy mismatch, leading them to be discarded from the sample used for the MCMC. The gaps around $z = 1$ and $z = 1.2$ likely represent mismatched supernovae clus-

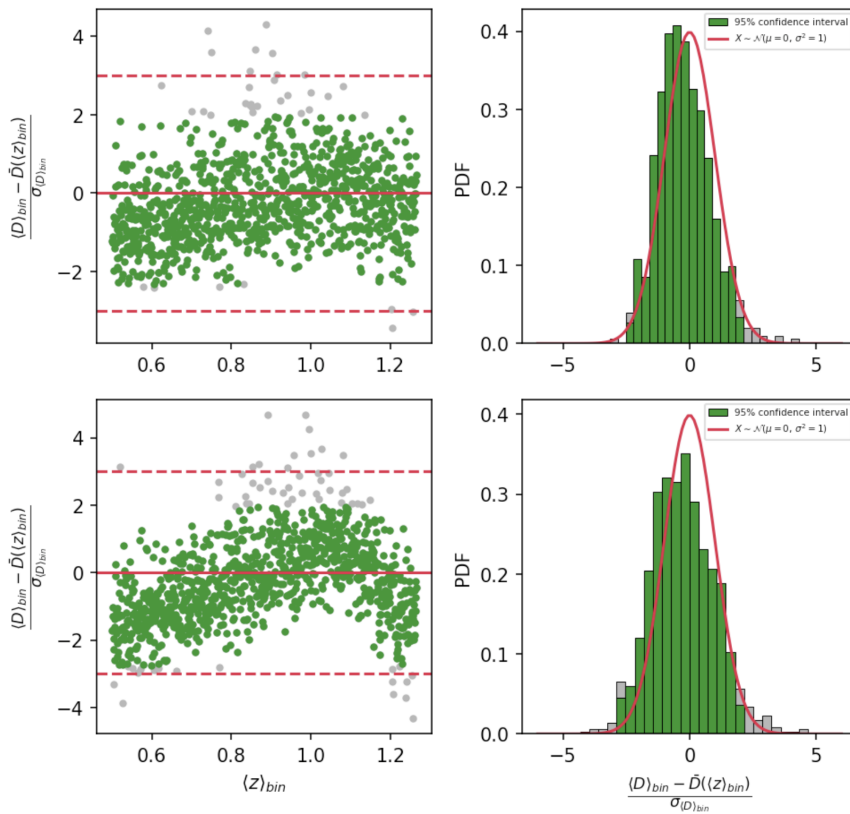


Figure 12: The upper panel shows the residuals of the MCMC fit performed under the assumption that the mismatching probability is proportional to θ . The lower panel shows the residuals of the MCMC fit in which all obstructed SNe Ia are mismatched to their foreground galaxy. The green sources correspond to those which are included in the 95% confidence interval of each residuals distribution.

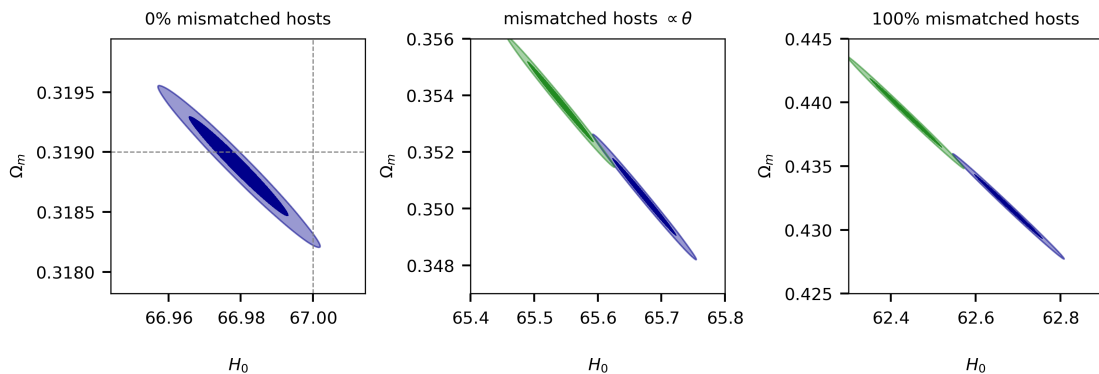


Figure 13: Constraints on H_0 and Ω_m for 3 different scenarios of obstructed supernovae mismatching. The blue ellipses correspond to the estimations which result from considering the entire random sample of SNe Ia while for the estimations represented by the green ellipses the outliers have been excluded from the sample.

tering at lower redshifts. This is substantiated by the fact that the regions neighbouring these gaps (around $z = 0.8$ and $z = 1$) are more densely populated as the fraction of mismatched supernovae increases.

Finally, we notice from the residual distributions that including mismatched supernovae in the fit leads to an increased number of outliers. To ensure that the shift observed in the central value of H_0 is not a consequence of these outliers only we exclude the outliers from the sample and run the MCMCs again for the two scenarios which account for mismatching. For each fit, the outliers are defined as supernovae lying outside the 95% confidence interval of the residual distribution. This verification is important since it is customary to exclude the outliers from the samples used to estimate cosmological parameters. As shown in Fig. 13, we find that removing outliers leads to a very similar shift in the central parameter values, which confirms that the misidentification of the host-galaxy of obstructed supernovae leads to a real bias of the measured value for H_0 .

6.3.3 Implication on the late-time H_0 estimation

The supernovae/host-galaxy matching algorithm currently used on observed SNe Ia samples is outlined in [20]. This algorithm follows a proximity-based matching approach, where the supernova and its host-galaxy are matched based on the projected distance from their positions only, without consideration for the third spatial dimension. The algorithm searches for galaxies located within a $30''$ radius around the supernova position. From this subsample of galaxies, the supernova is matched to the galaxy for which the normalized angular separation, considering the elliptical radius of the galaxy in the supernova's direction, is minimal (see [20] for a more thorough discussion on this procedure). The authors assert an accuracy rate of 97% for their supernova/host-galaxy matching algorithm. This result is based on testing the algorithm's performance using a simulated catalogue of $\sim 100\,000$ SNe Ia which are placed onto two different

samples of real observed galaxies in the redshift range $0.08 < z < 1.4$.

Several important considerations arise from these seemingly satisfactory results, which are particularly relevant in the context of the present study on the mismatch of obstructed supernovae. Firstly, all supernovae located at angular separations greater than $30''$ from the centre of their host-galaxies were removed from the simulated sample by the authors and therefore excluded from the matching process. Although these supernovae represent only a small subset of sources (0.05% in their first galaxy catalogue and 0.6% in their second galaxy catalogue), their removal likely leads to a slight overestimation of the algorithm's accuracy. In addition, due to their large separation from their host centres, these specific supernovae have a higher probability of being mismatched to their foreground galaxy, in case they are obstructed. Secondly, the authors find that the fraction of supernovae which are mismatched by their algorithm increases with redshift and that these supernovae are more often mismatched to galaxies with redshifts lower than their true redshift. As mentioned previously, the number of obstructed supernovae increases with redshift and the redshift of the foreground galaxy is always lower than that of the true host-galaxy. These results could therefore partly be attributed to the fact that their mismatched supernovae could be obstructed supernovae erroneously associated to their foreground galaxy.

The authors do not provide an estimation of the effect of host-galaxy misidentification on inferred cosmological parameter. However, as demonstrated by our results presented in the previous section, mismatching the obstructed SNe Ia only can already lead to a significant shift in H_0 . Considering these observations alongside our results, it is our belief that enhancing the performance of the SN Ia/host-galaxy matching algorithm and improving the accuracy of the resulting H_0 estimation could be accomplished by incorporating the consideration of supernova obstruction by foreground galaxies into the matching algorithm.

7 The impact of supernova blocking by the Milky Way on the estimation of H_0

This section is dedicated to evaluating the impact of the orientation of the Milky Way’s disk on the estimation of H_0 . Part of the sky is obstructed by the Milky Way’s disk, such that the supernovae lying behind the galactic disk cannot be observed. Since the Universe is neither perfectly homogeneous nor isotropic, the regions of the sky that are obstructed by the galactic disk can be more or less dense depending on the Milky Way’s orientation. In this section, we are interested in assessing whether the selection bias induced by this obstruction on the Hubble constant depends on the specific orientation of the Milky Way’s plane.

7.1 Supernova sample selection

The sources in the simulated catalogue only span the full sky up to $z = 0.1$. Therefore, in this part, we only take these low-redshift sources into account. As discussed in Section 3.1.1, peculiar motions, and more specifically coherent flows, lead to correlated systematic errors in low-redshift redshift measurements. However, these peculiar motions contaminate measurements beyond $z = 0.1$. Therefore, for the sample of sources considered in this section, it does not make sense to apply the low-redshift cut-off put forward in Section 3.1.3. In addition, below $z = 0.1$ there is relatively little intervening matter between the observer and the source. Galaxies at such low redshifts are therefore only slightly affected by gravitational lensing. This is why the binning procedure proposed in Section 3.1.3 to mitigate the bias induced by lensing is not applied to the SNe Ia samples used in this section either.

These low-redshift simulated SNe Ia are resampled to reproduce the redshift distribution of the *Pantheon+* supernova catalogue [35] used in the latest estimation of H_0 by the SH0ES team [31]. The *Pantheon+* catalogue comprises sources from 18 different surveys adding up to 1550 different SNe Ia in the redshift range $0.001 \leq z \leq 2.26$. The sources in this catalogue can be divided into 3 different subsets: at low redshift (up to $z = 0.1$), the observed supernovae span the full sky volume; at intermediate redshifts ($0.1 \leq z \leq 1.7$) the observed supernovae are contained in a plane oriented along $\theta = \pi/2$ as seen from our position; and at high redshift ($0.1 \leq z \leq 2.26$) the supernovae have been observed through multiple, conical shaped, “pencil beam” surveys. Resampling the $z \leq 0.1$ simulated sources to replicate the redshift distribution of the $z \leq 0.1$ *Pantheon+* sources allows us to estimate the impact that the specific orientation of the Milky Way plane would have on the estimation of H_0 if only the full-sky part of the *Pantheon+* catalogue were considered.

The orientation of the galactic plane is parameterized by its normal vector $\vec{n}_{GP} = [\theta, \phi]$. For 192 different orientations of \vec{n}_{GP} , we randomly select 5000 supernovae from the resampled low-redshift subsample of the simulated catalogue, which are not obstructed by the corresponding

galactic plane. More specifically, we consider that all supernovae which lie within $\pm 15^\circ$ of being orthogonal to \vec{n}_{GP} are blocked by the galactic disk. The Hubble constant is estimated from this sample of SNe Ia according to the method described in Section 3.2. Since the supernovae are not binned, the product in the likelihood function (Eq. 60) runs over the 5000 individual supernovae. In addition, we assume that the distance measurements of these supernovae all have the same error such that, in this case, σ_D is just a constant in the likelihood function.

7.2 Results

7.2.1 General features of the $H_0(\vec{n}_{GP})$ map

The Hubble constant is estimated for 192 different orientations of the galactic plane. The resulting map of $H_0(\vec{n}_{GP})$ is shown in Fig. 14. As seen from this map, the orientation of the galactic plane alone can cause a fluctuation in the Hubble constant estimated from the low redshift sources of ~ 0.9 km/s/Mpc. Therefore, if the Hubble constant is estimated from low-redshift supernovae only ($z \leq 0.1$), we find that the estimated value for H_0 is significantly affected by the specific orientation of the Milky Way disk.

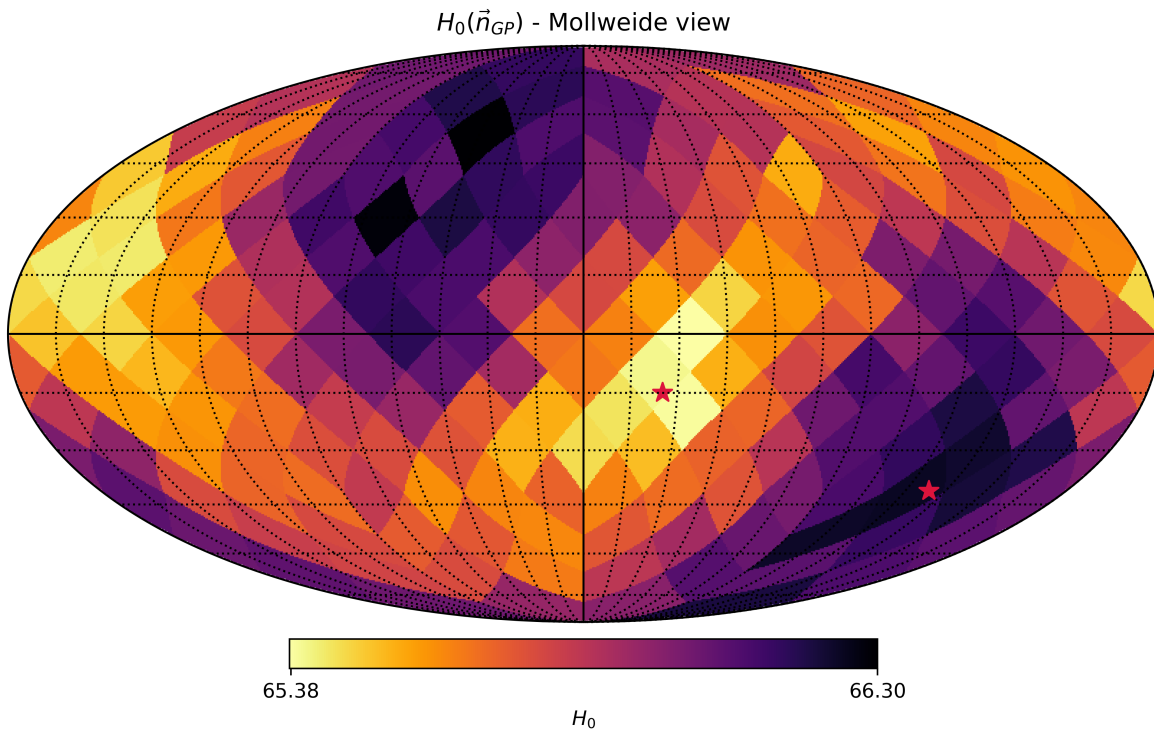


Figure 14: Map of H_0 as a function of the normal vector to the galactic plane \hat{n}_{GP} . The two stars represent the orientations of the normal vectors for which the estimated Hubble constant is minimal and maximal.

The vectors $\vec{n}_{GP} = [\theta, \phi]$ and $\vec{n}_{GP} = [\pi - \theta, \pi + \phi]$ are both normal to the same galactic plane orientation, which introduces the symmetry seen in the map of Fig. 14. Therefore, there are

two regions of high- H_0 and two regions of low- H_0 on this map which are in fact duplicates representing the same galactic planes.

The map of H_0 as a function of $\vec{n}_{GP} = [\theta, \phi]$ can be described mathematically through a multipole expansion. A multipole expansion corresponds to the series representation of an angle-dependent function. This series is most commonly written as a sum of spherical harmonics, since spherical harmonics form a complete set of orthogonal functions and therefore an ortho-normal basis of the Hilbert space. Therefore, any function defined on the surface of a sphere can be expanded as a linear combination of spherical harmonics

$$f(\theta, \phi) = \sum_{l=0}^{\infty} \sum_{m=-l}^l a_{lm} Y_{lm}(\theta, \phi). \quad (70)$$

In this expression, $Y_{lm}(\theta, \phi)$ is the spherical harmonic function of degree l and order m and a_{lm} is the corresponding spherical harmonics coefficient which depends on the function being expanded. Spherical harmonics satisfy the following conjugate symmetry property: $Y_{lm}^*(\theta, \phi) = (-1)^m Y_{l,-m}(\theta, \phi)$. If the function being expressed as a multipole expansion is real, the complex coefficients a_{lm} additionally have to satisfy the following reality condition: $a_{lm}^* = (-1)^m a_{l,-m}$, which follows from the conjugate symmetry of the spherical harmonic functions.

The degree l of a spherical harmonic indicates along how many axes the l -th multipole points. On the $H_0(\vec{n}_{GP})$ map in Fig. 14, two regions of minimal H_0 and two regions of maximal H_0 can be distinguished, which in 3D correspond to one axis of minimal H_0 and one axis of maximal H_0 . Therefore, the underlying function describing $H_0(\vec{n}_{GP})$ is dominated by the $l = 2$ (quadrupole) term of the multipole expansion.

7.2.2 Galactic plane orientations of extrema H_0

The orientation of the normal vectors \vec{n}_{GP}^{min} and \vec{n}_{GP}^{max} leading respectively to the minimal- H_0 and maximal- H_0 values on the $H_0(\vec{n}_{GP})$ map can be determined mathematically in order to find out which galactic plane orientations lead to maximal and minimal estimations of the Hubble constant.

To do so, we can make use of the fact that the l -th multipole term of a multipole expansion, $f_l(\theta, \phi)$, can be fully represented by a symmetric, traceless tensor of rank l . Such a tensor contains $2l + 1$ independent components which are linearly independent combinations of the a_{lm} coefficients of the expansion. This tensor therefore carries all the information of the multipole term encoded in a different way that allows to look for these “special directions” in the underlying function.

As given in [10], the general correspondence between the usual representation of a multipole

decomposition as defined in Eq. 70 and this tensor representation is

$$f_l(\vec{n}) = \sum_{m=-l}^l a_{lm} Y_{lm}(\vec{n}) = A^{(l)} \left\{ \prod_{i=1}^l (\hat{v}^{(l,i)} \cdot \hat{n}) - T_l \right\}. \quad (71)$$

In this expression, $A^{(l)}$ is a scalar associated with the amplitude of the l -th multipole term. The components of the unit vectors $\hat{v}^{(l,i)}$ are non-linear combinations of the a_{lm} coefficients of the decomposition for a fixed degree l (expressed in Cartesian coordinates). The vector \hat{n} corresponds to the radial unit vector in the $[\theta, \phi]$ -direction which in Cartesian coordinates is $\hat{n} = [\sin \theta \cos \phi, \sin \theta \sin \phi, \cos \theta]$. Finally, T_l is the sum of all traces of the first term. Subtracting T_l therefore renders the full expression traceless.

Based on this general definition, the tensor representation of the quadrupole term ($l = 2$) which describes the $H_0(\vec{n}_{GP})$ map is therefore given by

$$\sum_{m=-2}^2 a_{2m} Y_{2m}(\vec{n}) = A^{(2)} \left\{ (\hat{v}^{(2,1)} \cdot \hat{n}) (\hat{v}^{(2,2)} \cdot \hat{n}) - \frac{1}{3} \hat{v}^{(2,1)} \cdot \hat{v}^{(2,2)} \right\}. \quad (72)$$

The quadrupole vectors $\hat{v}^{(2,1)}$ and $\hat{v}^{(2,2)}$ each contain 2 independent pieces of information, which together with the amplitude $A^{(2)}$ are the $2l + 1 = 5$ pieces of information which fully specify the shape of the quadrupole.

Alternatively, the right-hand side of this equation can be rewritten as the quadratic form $F_Q(\hat{n})$ of a quadrupole matrix Q . The quadrupole matrix is a 3×3 symmetric, traceless matrix (corresponding to a tensor of rank $l = 2$) of the form

$$Q = \begin{bmatrix} Q_{11} & Q_{12} & Q_{13} \\ Q_{12} & Q_{22} & Q_{23} \\ Q_{13} & Q_{23} & -(Q_{11} + Q_{22}) \end{bmatrix}. \quad (73)$$

This matrix contains 5 independent which are 5 linearly independent combinations of the a_{2m} coefficients and fully specify the shape of the quadrupole. The quadratic form associated with this matrix is given by

$$F_Q(\hat{n}) = \hat{n}^T Q \hat{n}, \quad (74)$$

where $\hat{n} = [\sin \theta \cos \phi, \sin \theta \sin \phi, \cos \theta]$.

The tensor representation of the quadrupole term (Eq. 72) can therefore be rewritten as

$$\sum_{m=-2}^2 a_{2m} Y_{2m}(\vec{n}) = F_Q(\hat{n}). \quad (75)$$

By multiplying both sides of this equation with $\sum_{m=-2}^2 Y_{2m}^*(\vec{n})$, integrating and keeping only the non-vanishing terms we arrive at the following equation

$$a_{2m} \int_{\theta=0}^{\pi} \int_{\phi=0}^{2\pi} Y_{2m}(\theta, \phi) Y_{2m}^*(\theta, \phi) d\Omega = \int_{\theta=0}^{\pi} \int_{\phi=0}^{2\pi} F_Q(\theta, \phi) Y_{2m}^*(\theta, \phi) d\Omega. \quad (76)$$

Using the ortho-normality of spherical harmonics and the conjugate symmetry property introduced previously, this equation can be rewritten as

$$\begin{aligned} a_{2m} &= \int_{\theta=0}^{\pi} \int_{\phi=0}^{2\pi} F_Q(\theta, \phi) Y_{2m}^*(\theta, \phi) d\Omega \\ &= \int_{\theta=0}^{\pi} \int_{\phi=0}^{2\pi} F_Q(\theta, \phi) (-1)^m Y_{2,-m}(\theta, \phi) d\Omega. \end{aligned} \quad (77)$$

We therefore find at the following equations for a_{20} , a_{21} and a_{22} :

$$\begin{aligned} a_{20} &= \int_{\theta=0}^{\pi} \int_{\phi=0}^{2\pi} F_Q(\theta, \phi) Y_{2,0}(\theta, \phi) d\Omega, \\ a_{21} &= - \int_{\theta=0}^{\pi} \int_{\phi=0}^{2\pi} F_Q(\theta, \phi) Y_{2,-1}(\theta, \phi) d\Omega, \\ a_{22} &= \int_{\theta=0}^{\pi} \int_{\phi=0}^{2\pi} F_Q(\theta, \phi) Y_{2,-2}(\theta, \phi) d\Omega. \end{aligned} \quad (78)$$

By computing these integrals we find the following relation between the real and imaginary parts of the spherical harmonic coefficients and the components of the quadrupole matrix

$$\begin{aligned} a_{20}^{re} &= -2\sqrt{\frac{\pi}{5}} (Q_{11} + Q_{22}) & a_{20}^{im} &= 0 \\ a_{21}^{re} &= -2\sqrt{\frac{2\pi}{15}} Q_{13} & a_{21}^{im} &= -2\sqrt{\frac{2\pi}{15}} Q_{32} \\ a_{22}^{re} &= \sqrt{\frac{2\pi}{15}} (Q_{11} - Q_{22}) & a_{22}^{im} &= -2\sqrt{\frac{2\pi}{15}} Q_{12} \end{aligned} \quad (79)$$

These equations can be inverted to find the expressions for the components of the quadrupole matrix in terms of the spherical harmonic coefficients

$$Q = \begin{bmatrix} -\frac{1}{4}\sqrt{\frac{5}{\pi}}(a_{20}^{re} - \sqrt{6}a_{22}^{re}) & -\frac{1}{2}\sqrt{\frac{15}{2\pi}}a_{22}^{im} & -\frac{1}{2}\sqrt{\frac{15}{2\pi}}a_{21}^{re} \\ -\frac{1}{2}\sqrt{\frac{15}{2\pi}}a_{22}^{im} & -\frac{1}{4}\sqrt{\frac{5}{\pi}}(a_{20}^{re} + \sqrt{6}a_{22}^{re}) & \frac{1}{2}\sqrt{\frac{15}{2\pi}}a_{21}^{im} \\ -\frac{1}{2}\sqrt{\frac{15}{2\pi}}a_{21}^{re} & \frac{1}{2}\sqrt{\frac{15}{2\pi}}a_{21}^{im} & \frac{1}{2}\sqrt{\frac{5}{\pi}}a_{20}^{re} \end{bmatrix}. \quad (80)$$

(Note that since the a_{2m} coefficients satisfy the reality condition introduced previously, the coefficients $a_{2,-2}$ and $a_{2,-1}$ can be expressed in terms of $a_{2,2}$ and $a_{2,12}$ and don't contain any additional information.)

The `healpy` package includes a function which returns the a_{lm} coefficients of the spherical harmonic decomposition of a HEALPix map. Using this tool, we find the following spherical

harmonic coefficients for the $H_0(\vec{n}_{GP})$ map

$$\begin{aligned}
 a_{20}^{re} &= 0.199 & a_{20}^{im} &= 0 \\
 a_{21}^{re} &= -0.23 & a_{21}^{im} &= 0.223 \\
 a_{22}^{re} &= -0.148 & a_{22}^{im} &= -0.316.
 \end{aligned}
 \tag{81}$$

Since Q is a real, symmetric matrix, the directions of the minimum and maximum of the function describing the $H_0(\vec{n}_{GP}[\theta, \phi])$ map are given respectively by the eigenvector associated with the smallest and largest eigenvalues of this quadrupole matrix. (See the Appendix for the mathematical proof of this statement.) Substituting the spherical harmonics coefficients of Eq. 81 in the quadrupole matrix of Eq. 80 we find the following eigenvectors whose direction correspond to the normal vector to the galactic plane resulting in the maximum and minimum value of $H_0(\vec{n}_{GP})$

$$\begin{aligned}
 \vec{v}_{GP}^{max} &= [\theta_{max} = 2.29 \text{ rad}, \phi_{max} = 4.04 \text{ rad}] \\
 \vec{v}_{GP}^{min} &= [\theta_{min} = 1.83 \text{ rad}, \phi_{min} = 5.84 \text{ rad}].
 \end{aligned}
 \tag{82}$$

Therefore, a galactic plane orientation normal to $\vec{v}_{min} = [1.83 \text{ rad}, 5.84 \text{ rad}]$ leads to an estimate of $H_0 = 65.38 \text{ km/s/Mpc}$ while a galactic plane normal to $\vec{v}_{max} = [2.29 \text{ rad}, 4.04 \text{ rad}]$ leads to an estimate of $H_0 = 66.29 \text{ km/s/Mpc}$.

7.3 Discussion

The anisotropic expansion rate that arises from the obstruction of low-redshift supernovae by the Milky Way's disk can be attributed to the structure of the neighbouring Universe, which gives rise to local flows. As mentioned in Section 3.1.1, the perturbations in the Universe's density field are associated with perturbations in the gravitational field which deflect galaxies from the uniform motion dictated by the Hubble flow. These peculiar motions lead groups of galaxies (and the supernovae they host) to fall into larger galaxy clusters or superclusters. These groups of galaxies which conjointly move in coherent flows therefore tend to have correlated peculiar velocities, introducing correlated systematic errors in the Hubble diagram. This effect is particularly strong in the low-redshift region of the Hubble diagram, where the supernovae are physically closer to each other as a function of their angular separation on the sky. Therefore, the low-redshift sources that are obstructed by the Milky Way, for each of the disk orientations simulated, are strongly correlated to each other. Removing these obstructed, correlated supernovae from the Hubble diagram used to determine H_0 therefore introduces a bias in the estimation due to the non-random nature of their exclusion. This bias varies slightly for each orientation of the Milky Way's disk, resulting in the anisotropic $H_0(\vec{n}_{GP})$ map. The quadrupole effect that we find in the H_0 map is therefore a direct consequence of the high-order multipole effect in the local inhomogeneous velocity field.

When the estimation of the Hubble constant relies purely on supernovae at (very) low redshifts ($z \leq 0.1$), the specific orientation of the Milky Way disk has a significant impact on the resulting value of H_0 . However, we anticipate that this bias becomes negligible once sources at higher redshifts are also included in the analysis. This expectation seems reasonable since at higher redshifts, sources lie at increasingly large physical distances from each other relative to their angular separations on the sky. We therefore expect that the correlation among supernovae blocked by the Milky Way diminishes at higher redshifts. Moreover, higher redshifts also span larger cosmic volumes, leading to a larger number of sources. These combined factors therefore imply that when high-redshift sources are incorporated into the H_0 estimation, the exclusion of blocked supernovae from the Hubble diagram becomes more akin to excluding a random sample, resulting in a smaller bias in the inferred value for H_0 .

This suggests that the blocking of supernovae by the Milky Way's disk does not introduce a significant bias in H_0 when using observed supernova samples like the *Pantheon+* catalogue, which includes sources up to $z = 2.26$, as long as the analysis does not rely solely on the low-redshift full-sky portion of the catalogue. We cannot verify this using the simulated supernova catalogue used for this study as its full-sky part only extends to $z = 0.1$. However, this is definitely something that should be verified using a simulated sample of sources which spans the full-sky volume at higher redshifts as well.

Nevertheless, addressing the bias introduced by these low-redshift correlated supernovae remains important, even if their impact on H_0 is expected to be negligible. This is because they compromise the assumptions underlying the likelihood function employed in the MCMC analysis. As discussed previously, this bias can simply be averted by introducing a low-redshift cut-off or, in a more systematic way, by incorporating the velocity covariance in the likelihood analysis to down-weight the low-redshift supernovae.

8 Conclusion

Despite considerable efforts, a compelling explanation of the persistent discrepancy between early-time and late-time measurements of the Hubble constant remains yet to be found. Some interpret this Hubble tension as a harbinger for new physics beyond the concordance Λ CDM model. However, the alternative cosmological models proposed thus far have not proven to be satisfactory substitutes. In this context, we believe it is not only relevant, but imperative to continue to look for new sources of bias in our late-Universe H_0 measurements, performed under the assumption of the Λ CDM model. The leading method to estimate the Hubble constant in the local Universe is based on the Type Ia supernovae distance ladder. In this respect, this work assesses how the blocking of certain supernovae by foreground galaxies can bias our late-time estimation of the Hubble constant. We find that 2.4% to 9% of the supernovae in our simulated catalogue are obstructed by a foreground galaxy, depending on the way in which we define the effective radius of a galaxy. Most of these sources are obstructed by a neighbouring galaxy located in the same galaxy cluster as their host-galaxy and they are, on average, more magnified than their visible counterparts.

In its simplest form, this blocking implies that supernovae lying behind a foreground galaxy are excluded from our observed samples. We find that this selection bias leads to an overestimation of H_0 which ranges from 0.03% to 0.09% depending on the chosen definition for galactic radii. Currently, the impact of this selection bias is not substantial, given the precision of existing H_0 estimations. However, with the forthcoming launch of upcoming surveys such as the LSST, we anticipate a significant increase in the size of supernovae samples. This will likely shift the dominant source of error in SNe Ia distance measurements from statistical errors to systematic errors emphasising the need for more robust consideration of systematic biases. Consequently, smaller systematic errors, including the selection bias discussed here, will therefore gain importance and require more attention in the upcoming years. Nonetheless, the presented estimates of the fraction of obstructed supernovae can be regarded as conservative, suggesting that the impact of this selection bias is likely to be more prominent in observed samples of supernovae.

To date, the primary focus of improving the SNe Ia distance ladder has been increasing the accuracy and precision with which we can determine the luminosity of supernovae, and thus their use as reliable standard candles. In contrast, error of the indirect determination of supernovae's redshift through that of their host-galaxy has received less attention, often being regarded as negligible. However, we show here that supernova blocking can also have an impact on these redshift determinations, namely if obstructed supernovae are erroneously assigned the redshift of their foreground galaxy instead of that of their host-galaxy. We find that such host-galaxy misidentifications can result in an underestimation of H_0 of the order of 1.95% in the scenario where the mismatch probability is proportional to the angular separation between the

obstructed supernova and its foreground galaxy. This represents a non-negligible shift in the central value of H_0 , indicating the importance of further investigation into the impact of this mismatching using observed supernova samples.

Lastly, we examine the selection bias induced by the specific orientation of the Milky Way's plane on the estimation of the Hubble constant. Our analysis reveals that this selection bias is quite significant when the measurement of the Hubble constant relies on low redshift sources only ($z \leq 0.1$), as it can lead to a shift in the central value of H_0 of ~ 0.9 km/s/Mpc. However, once higher redshift sources are included into the analysis as well, it is expected that this bias becomes negligible.

The overall bias resulting from supernova blocking is a combination of these three effects, with the misidentification of the host-galaxies of obstructed sources being the dominant component. We therefore conclude that further efforts to improve the accuracy of our late-time estimation of the Hubble constant should include two important steps. Firstly, incorporating the consideration of host misidentification of obstructed supernovae in our matching algorithms. Secondly, correcting for the selection bias induced by total supernovae blocking when we reach larger observed supernovae samples. Finally, our analysis reveals that while certain errors remaining in our late-time estimation of the Hubble constant could potentially alleviate the Hubble tension, others might also aggravate it. Therefore, the results presented here also substantiate the fact that it seems unlikely that unrelated systematic errors alone can resolve this tension.

A Extrema of the linear map described by a matrix

We consider a (real) matrix M which represents a linear map and a vector \vec{v} . The Rayleigh quotient of M and \vec{v} is defined as

$$R_M(\vec{v}) = \frac{\|M\vec{v}\|^2}{\|\vec{v}\|^2} = \frac{\vec{v}^T M \vec{v}}{\vec{v}^T \vec{v}} \quad (83)$$

The Rayleigh quotient of a matrix and a vector represents the ‘‘amplifying effect’’ of the linear map represented by the matrix M on the vector \vec{v} . Therefore, the maximum (resp. minimum) of the linear map is in the direction on the vector \vec{v}_{max} (resp. \vec{v}_{min}) for which the Rayleigh quotient is maximized (resp. minimized). The amplitude of this maximum (resp. minimum) is given by the value of the Rayleigh quotient for \vec{v}_{max} (resp. \vec{v}_{min}).

Suppose that M is a symmetric $n \times n$ matrix and let $\{\lambda_1, \dots, \lambda_n\}$ be its eigenvalues. Since M is a real, symmetric matrix, there exists an ortho-normal basis $\{\hat{e}_1, \dots, \hat{e}_n\}$ of R^n where \hat{e}_i is the eigenvector associated with λ_i .

Since $\{\hat{e}_1, \dots, \hat{e}_n\}$ of R^n form an ortho-normal basis for R^n , any vector $\vec{v} \in R^n$ can be rewritten uniquely in terms of this ortho-normal basis and a set of coefficients α_i as

$$\vec{v} = \sum_{i=1}^n \alpha_i \hat{e}_i. \quad (84)$$

In addition, since $R_M(\vec{v})$ does not depend on the norm of \vec{v} , we can impose the constraint $\|\vec{v}\|^2 = 1$.

We can therefore rewrite

$$\vec{v}^T \vec{v} = \left(\sum_{i=1}^n \alpha_i \hat{e}_i \right)^T \left(\sum_{i=1}^n \alpha_i \hat{e}_i \right) = \sum_{i=1}^n \alpha_i^2, \quad (85)$$

$$\vec{v}^T M \vec{v} = \left(\sum_{i=1}^n \alpha_i \hat{e}_i \right)^T \left(\sum_{i=1}^n \alpha_i \lambda_i \hat{e}_i \right) = \sum_{i=1}^n \alpha_i^2 \lambda_i. \quad (86)$$

The Rayleigh quotient therefore becomes

$$R_M(\vec{v}) = \frac{\sum_{i=1}^n \alpha_i^2 \lambda_i}{\sum_{i=1}^n \alpha_i^2}. \quad (87)$$

This quotient is a weighted average of the eigenvalues with weight α_i^2 summing to 1. Suppose the k -th eigenvalue is the largest. The Rayleigh quotient will then be maximized if the weight on λ_k is $\alpha_k^2 = 1$ and $\alpha_{i \neq k}^2 = 0$ for all other terms. Such a vector is a basis vector, namely the

eigenvector corresponding to the largest eigenvalue. The maximum of the linear map described by the matrix is therefore in the direction of the eigenvector associated with the largest eigenvalue.

For the same reasons, the minimum of the linear map described by the matrix is therefore in the direction of the eigenvector associated with the smallest eigenvalue.

References

- [1] K. N. Abazajian et al. “The Seventh Data Release of the Sloan Digital Sky Survey”. In: *The Astrophysical Journal Supplement Series* 182.2 (2009), pp. 543–558. DOI: [10.1088/0067-0049/182/2/543](https://doi.org/10.1088/0067-0049/182/2/543).
- [2] J. Adamek et al. “Bias and scatter in the Hubble diagram from cosmological large-scale structure”. In: *Physical Review D* 100.2 (2019). DOI: [10.1103/physrevd.100.021301](https://doi.org/10.1103/physrevd.100.021301).
- [3] J. Adamek et al. “gevolution: a cosmological N-body code based on General Relativity”. In: *Journal of Cosmology and Astroparticle Physics* 2016.07 (2016), pp. 053–053. DOI: [10.1088/1475-7516/2016/07/053](https://doi.org/10.1088/1475-7516/2016/07/053).
- [4] S. Alam et al. “Completed SDSS-IV extended Baryon Oscillation Spectroscopic Survey: Cosmological implications from two decades of spectroscopic surveys at the Apache Point Observatory”. In: *Physical Review D* 103.8 (2021). DOI: [10.1103/physrevd.103.083533](https://doi.org/10.1103/physrevd.103.083533).
- [5] P.S. Behroozi, R.H. Wechsler, and H. Wu. “The Rockstar Phase-Space Temporal Halo Finder and the Velocity Offsets of Cluster Cores”. In: *The Astrophysical Journal* 762.2 (2012), p. 109. DOI: [10.1088/0004-637x/762/2/109](https://doi.org/10.1088/0004-637x/762/2/109).
- [6] S. Birrer et al. “TDCOSMO IV: Hierarchical time-delay cosmography – joint inference of the Hubble constant and galaxy density profiles”. In: *Astronomy & Astrophysics* 643 (2020), A165. DOI: [10.1051/0004-6361/202038861](https://doi.org/10.1051/0004-6361/202038861).
- [7] D. Branch and D.L. Miller. “Type IA Supernovae as Standard Candles”. In: *Astrophysical Journal Letters* 405 (1993), p. L5. DOI: [10.1086/186752](https://doi.org/10.1086/186752).
- [8] D. Brout et al. “The Pantheon+ Analysis: Cosmological Constraints”. In: *The Astrophysical Journal* 938.2 (2022), p. 110. DOI: [10.3847/1538-4357/ac8e04](https://doi.org/10.3847/1538-4357/ac8e04).
- [9] A. Carr et al. “The Pantheon+ analysis: Improving the redshifts and peculiar velocities of Type Ia supernovae used in cosmological analyses”. In: *Publications of the Astronomical Society of Australia* 39 (2022). DOI: [10.1017/pasa.2022.41](https://doi.org/10.1017/pasa.2022.41).
- [10] C.J. Copi et al. “On the large-angle anomalies of the microwave sky”. In: *Monthly Notices of the Royal Astronomical Society* 367.1 (2006), pp. 79–102. DOI: [10.1111/j.1365-2966.2005.09980.x](https://doi.org/10.1111/j.1365-2966.2005.09980.x).
- [11] T.M. Davis et al. “Can redshift errors bias measurements of the Hubble Constant?” In: *Monthly Notices of the Royal Astronomical Society* 490.2 (2019), pp. 2948–2957. DOI: [10.1093/mnras/stz2652](https://doi.org/10.1093/mnras/stz2652).
- [12] T.M. Davis et al. “The effect of peculiar velocities on supernova cosmology”. In: *The Astrophysical Journal* 741.1 (2011), p. 67. DOI: [10.1088/0004-637x/741/1/67](https://doi.org/10.1088/0004-637x/741/1/67).
- [13] P. Denzel et al. “The Hubble constant from eight time-delay galaxy lenses”. In: *Monthly Notices of the Royal Astronomical Society* 501.1 (2020), pp. 784–801. DOI: [10.1093/mnras/staa3603](https://doi.org/10.1093/mnras/staa3603).

REFERENCES

- [14] S. Dodelson. *Modern Cosmology*. Academic Press, 2003. ISBN: 978-0-12-219141-1.
- [15] P. Fleury, C. Clarkson, and R. Maartens. “How does the cosmic large-scale structure bias the Hubble diagram?” In: *Journal of Cosmology and Astroparticle Physics* 2017.03 (2017), pp. 062–062. DOI: [10.1088/1475-7516/2017/03/062](https://doi.org/10.1088/1475-7516/2017/03/062).
- [16] R.J. Foley et al. “The Foundation Supernova Survey: motivation, design, implementation, and first data release”. In: *Monthly Notices of the Royal Astronomical Society* 475.1 (2017), pp. 193–219. DOI: [10.1093/mnras/stx3136](https://doi.org/10.1093/mnras/stx3136).
- [17] D. Foreman-Mackey et al. “Emcee: The MCMC Hammer”. In: *Publications of the Astronomical Society of the Pacific* 125.925 (2013), pp. 306–312. DOI: [10.1086/670067](https://doi.org/10.1086/670067).
- [18] A. Gelman et al. *Bayesian Data Analysis*. Chapman and Hall/CRC, 2004. ISBN: 978-1-43-984095-5.
- [19] J. Goodman and J. Weare. “Multivariate Density Estimation: Theory, Practice, and Visualization”. In: *Communications in Applied Mathematics and Computational Science* 5.1 (2010), pp. 65–80. DOI: [10.2140/camcos.2010.5.65](https://doi.org/10.2140/camcos.2010.5.65).
- [20] R.R. Gupta et al. “Host galaxy identification for supernova surveys”. In: *The Astronomical Journal* 152.6 (2016), p. 154. DOI: [10.3847/0004-6256/152/6/154](https://doi.org/10.3847/0004-6256/152/6/154).
- [21] D.E. Holz and E.V. Linder. “Safety in Numbers: Gravitational Lensing Degradation of the Luminosity Distance-Redshift Relation”. In: *The Astrophysical Journal* 631.2 (2005), pp. 678–688. DOI: [10.1086/432085](https://doi.org/10.1086/432085).
- [22] E. Hubble. “A Relation between Distance and Radial Velocity among Extra-Galactic Nebulae”. In: *Proceedings of the National Academy of Science* 15.3 (1929), pp. 168–173. DOI: [10.1073/pnas.15.3.168](https://doi.org/10.1073/pnas.15.3.168).
- [23] E. Kourkchi et al. “Cosmicflows-4: The Calibration of Optical and Infrared Tully–Fisher Relations”. In: *The Astrophysical Journal* 896.1 (2020), p. 3. DOI: [10.3847/1538-4357/ab901c](https://doi.org/10.3847/1538-4357/ab901c).
- [24] H.S. Leavitt and E.C. Pickering. “Periods of 25 Variable Stars in the Small Magellanic Cloud”. In: *Harvard College Observatory Circular* 173 (1912), pp. 1–3.
- [25] G. Lemaître. “Un Univers homogène de masse constante et de rayon croissant rendant compte de la vitesse radiale des nébuleuses extra-galactiques”. In: *Annales de la Société Scientifique de Bruxelles* A47 (1927), pp. 49–59.
- [26] P.J.E. Peebles. *Principles of Physical Cosmology*. Princeton University Press, 1993. ISBN: 978-0-69-120672-1.
- [27] E.R. Peterson et al. “The Pantheon+ Analysis: Evaluating Peculiar Velocity Corrections in Cosmological Analyses with Nearby Type Ia Supernovae”. In: *The Astrophysical Journal* 938.2 (2022), p. 112. DOI: [10.3847/1538-4357/ac4698](https://doi.org/10.3847/1538-4357/ac4698).
- [28] M.M. Phillips et al. “The Reddening-Free Decline Rate Versus Luminosity Relationship for Type Ia Supernovae”. In: *The Astronomical Journal* 118.4 (1999), pp. 1766–1776. DOI: [10.1086/301032](https://doi.org/10.1086/301032).

REFERENCES

- [29] Planck Collaboration et al. “Planck 2015 results. XIII. Cosmological parameters”. In: *Astronomy & Astrophysics* 594 (2016), A13. DOI: [10.1051/0004-6361/201525830](https://doi.org/10.1051/0004-6361/201525830).
- [30] Planck Collaboration et al. “Planck 2018 results. VI. Cosmological parameters”. In: *Astronomy & Astrophysics* 641 (2020), A6. DOI: [10.1051/0004-6361/201833910](https://doi.org/10.1051/0004-6361/201833910).
- [31] A.G. Riess et al. “A Comprehensive Measurement of the Local Value of the Hubble Constant with 1 km/s/Mpc Uncertainty from the Hubble Space Telescope and the SH0ES Team”. In: *The Astrophysical Journal Letters* 934.1 (2022), p. L7. DOI: [10.3847/2041-8213/ac5c5b](https://doi.org/10.3847/2041-8213/ac5c5b).
- [32] A.G. Riess et al. “Cosmic Distances Calibrated to 1% Precision with Gaia EDR3 Parallaxes and Hubble Space Telescope Photometry of 75 Milky Way Cepheids Confirm Tension with Λ CDM”. In: *The Astrophysical Journal Letters* 908.1 (2021), p. L6. DOI: [10.3847/2041-8213/abdbaf](https://doi.org/10.3847/2041-8213/abdbaf).
- [33] A.G. Riess et al. “Type Ia Supernova Distances at Redshift > 1.5 from the Hubble Space Telescope Multi-cycle Treasury Programs: The Early Expansion Rate”. In: *The Astrophysical Journal* 853.2 (2018), p. 126. DOI: [10.3847/1538-4357/aaa5a9](https://doi.org/10.3847/1538-4357/aaa5a9).
- [34] J. Schombert, S. McGaugh, and F. Lelli. “Using the Baryonic Tully-Fisher Relation to Measure H_0 ”. In: *The Astronomical Journal* 160.2 (2020), p. 71. DOI: [10.3847/1538-3881/ab9d88](https://doi.org/10.3847/1538-3881/ab9d88).
- [35] D. Scolnic et al. “The Pantheon+ Analysis: The Full Data Set and Light-curve Release”. In: *The Astrophysical Journal* 938.2 (2022), p. 113. DOI: [10.3847/1538-4357/ac8b7a](https://doi.org/10.3847/1538-4357/ac8b7a).
- [36] M. Tanabashi et al. “Review of Particle Physics”. In: *Physical Review D* 98 (3 2018), p. 030001. DOI: [10.1103/PhysRevD.98.030001](https://doi.org/10.1103/PhysRevD.98.030001).
- [37] E. Di Valentino et al. “In the realm of the Hubble tension — a review of solutions”. In: *Classical and Quantum Gravity* 38.15 (2021), p. 153001. DOI: [10.1088/1361-6382/ac086d](https://doi.org/10.1088/1361-6382/ac086d).
- [38] S. Weinberg. *Cosmology*. Oxford University Press, 2008. ISBN: 978-0-19-852682-7.
- [39] T. Yang, S. Birrer, and B. Hu. “The first simultaneous measurement of Hubble constant and post-Newtonian parameter from time-delay strong lensing”. In: *Monthly Notices of the Royal Astronomical Society: Letters* 497.1 (2020), pp. L56–L61. DOI: [10.1093/mnrasl/slaa107](https://doi.org/10.1093/mnrasl/slaa107).
- [40] J. Yoo. *Lecture notes in Physical Cosmology (AST513)*. 2022. URL: <https://www.ics.uzh.ch/~jyoo/class/2022/TC2022.pdf>.